Squeeze3D: Extreme Neural Compression with Latent Space Bridging

Rishit Dagli *rishit@cs.toronto.edu*
University of Toronto and Vector Institute

Yushi Guan *guanyushi@cs.toronto.edu*
University of Toronto and Vector Institute

Sankeerth Durvasula *sankeerth@cs.toronto.edu*
University of Toronto and Vector Institute

Mohammadreza Mofayezi *mofayezi@cs.toronto.edu*
University of Toronto and Vector Institute

Nandita Vijaykumar *nandita@cs.toronto.edu*
University of Toronto and Vector Institute

https://squeeze3d.github.io

Reviewed on OpenReview: https://openreview.net/forum?id=XXYGHfqzvA

arXiv:2506.07932v2 [cs.GR] 28 Sep 2026

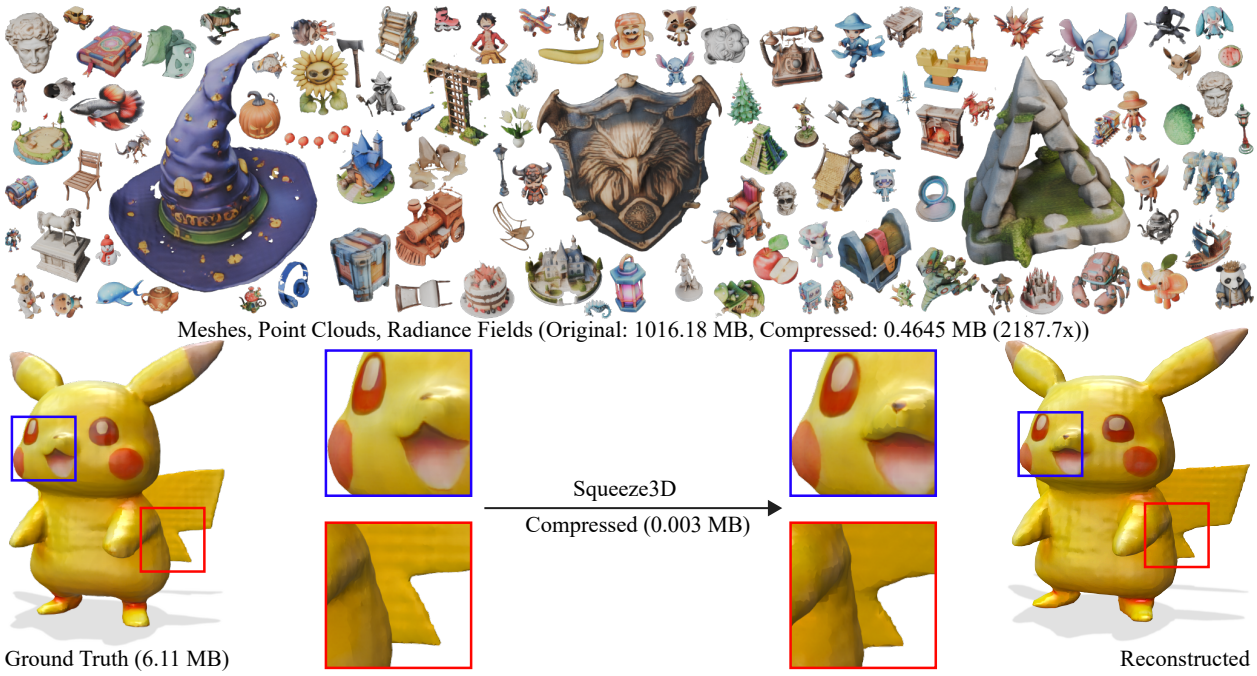


Figure 1: **Squeeze3D** allows for extreme compression of 3D models while preserving perceptual quality. *Top:* Our method compresses a diverse collection of 3D models. *Bottom:* Comparison between the original model (6.11 MB) and the reconstruction after compression (0.003 MB).

Abstract

We propose SQUEEZE3D, a novel framework that leverages implicit prior knowledge learnt by existing pre-trained encoders and decoders to compress 3D data at extremely high compression

ratios. Our approach bridges the latent spaces between a pre-trained encoder and a pre-trained decoder model through trainable mapping networks. Any 3D asset represented as a mesh, point cloud, or radiance field is first encoded by the pre-trained encoder and then transformed (*i.e. compressed*) into a highly compact latent code by a mapping network. This latent code can effectively be used as an extremely compressed representation of the mesh, point cloud, or radiance field. A mapping network transforms the compressed latent code into the latent space of a powerful generative model; the decoder of this generative model then recreates the original 3D asset (*i.e. decompression*). SQUEEZE3D is trained entirely on generated synthetic data and does not require any 3D datasets. The SQUEEZE3D architecture can be flexibly used with existing pre-trained 3D encoders and existing generative models. It can flexibly support different formats, including meshes, point clouds, and radiance fields. Our experiments demonstrate that SQUEEZE3D achieves compression ratios of up to 2187× for textured meshes, 58.5× for point clouds, and more than 650× for radiance fields while maintaining visual quality comparable to many existing methods. SQUEEZE3D only incurs a small compression and decompression latency since it does not involve training object-specific networks to compress an object.

1 Introduction

The rapid advancement of 3D data acquisition and representation technologies over the past decade has significantly expanded the availability and generation of high-resolution 3D content across various domains in different formats, including meshes, point clouds, and radiance fields (which could be extracted from a NeRF (Mildenhall et al., 2021) or a 3DGS (Kerbl et al., 2023)). The widespread use of 3D data necessitates the development of techniques that enable efficient transmission, storage, and processing of large-scale 3D representations. To this end, *compression* and the use of *compressed representations* for 3D data are of utmost importance, e.g., in streaming, autonomous navigation, digital twins, remote sensing.

A large body of work proposes techniques to compress meshes, point clouds, neural radiance fields (NeRFs) (Mildenhall et al., 2021), and 3D Gaussian Splats (3DGS) (Kerbl et al., 2023). These approaches aim to maximize the compression ratio while retaining reconstruction quality. For example, traditional mesh decimation techniques (Schroeder et al., 1992; Garland & Heckbert, 1997; Li et al., 2014; Lescoat et al., 2020) remain foundational for polygon reduction, but their reliance on handcrafted simplification rules limits their ability to preserve fine geometric details at extreme compression ratios. MPEG's G-PCC and V-PCC standards (Schwarz et al., 2018; Liu et al., 2019) use projection-based methods for point cloud compression; however, these approaches incur overheads for representing fine details and packing. Prior works also propose a range of compression methods for NeRFs (Li et al., 2024; Edavamadathil Sivaram et al., 2024; Takikawa et al., 2022; Müller et al., 2022) or 3DGS models (Fan et al., 2024; Lee et al., 2024). Several works propose autoencoder-style networks that compress 3D models into small latent vectors (Zhang et al., 2025a; Hahner & Garcke, 2022; Zhou et al., 2020; Chen et al., 2025a). The maximum compression ratios achieved by these methods are of the order of 100× for meshes and of the order of 10× for point clouds, but typically much lower.

Our goal is to develop a framework for *extreme* compression of 3D data stored in any format while retaining high visual quality. We emphasize that SQUEEZE3D is designed to compress *arbitrary, real-world* 3D assets (e.g., artist-created meshes and 3D scans). Such extreme ratios are most valuable at scale: streaming or archiving collections of millions of 3D assets, delivering content to bandwidth-constrained or on-device clients, and settings where the decoder is a shared, one-time asset that is amortized across all compressed objects (Section 4.7). Recent years have seen significant and continued advances and development of powerful generative models. In this work, we aim to leverage the implicit prior knowledge learnt by the decoders of powerful 3D generative models (Xu et al., 2024; Jun & Nichol, 2023) to enable extreme compression ratios. Recent works also propose techniques to leverage generative models for 3D compression (Zhang et al., 2024a; Cui et al., 2025; Zhang et al., 2025a; van den Oord et al., 2017; Zhang et al., 2025b; Chang et al., 2025; Roessle et al., 2024), and one achieves extreme compression for meshes (Zhang et al., 2024a). However, these approaches require training specialized encoders and generative models for a single 3D format. In contrast, our

goal is to flexibly use *existing* encoders and decoder models that provide adaptability as encoders/generative models evolve and flexibility across 3D formats.

We propose SQUEEZE3D, a compression framework that generates a highly compressed latent vector that can be used to recreate the original 3D data using an existing pre-trained decoder model. SQUEEZE3D comprises three key components: (1) the input 3D data is encoded with a pre-trained encoder. This allows us to extend SQUEEZE3D to other 3D encoders. (2) We train two small neural networks that we call the *forward mapping network* and the *reverse mapping network*. The forward mapping network maps the encoded representations into an extremely compressed latent space. The reverse mapping network converts the code from the compressed latent space to the latent space of the generative model. (3) We use a pre-trained decoder of a generation model to generate the original 3D data using the code generated by the reverse mapping network. SQUEEZE3D can be flexibly implemented with any pre-trained encoder and decoder of a generative model.

The forward and reverse mapping networks are trained for any given encoder-generator pair. We first synthetically generate a 3D dataset via random prompts to the generator model. This 3D dataset is encoded using the pre-trained encoder. The set of latents produced from the pre-trained encoders (training inputs) and their corresponding latents from the pre-trained generator (ground truth) are used to train the forward and reverse mapping networks. We propose a loss function that minimizes redundant information in the compressed latent space.

SQUEEZE3D can be flexibly applied to 3D data in different formats. We implement and evaluate our method for mesh, point cloud, and radiance field compression using 3 existing encoders and 5 existing generative models. We demonstrate that our method achieves compression ratios significantly higher than or on par with those of existing compression techniques for meshes, point clouds, and radiance fields, with reconstruction quality that is on par with many prior approaches. We demonstrate a compression ratio of 2187× for a subset of the Objaverse (Deitke et al., 2023) dataset, 58.5× on a subset of ShapeNet (Chang et al., 2015), and more than 650× across our radiance-field evaluations (Irshad et al., 2024). While SQUEEZE3D expectedly cannot achieve state-of-the-art reconstruction quality, we qualitatively show that it is able to retain high visual quality in many settings.

Contributions. (1) To the best of our knowledge, this is the first framework that leverages *pre-existing, pre-trained* generative-model decoders to enable extreme compression of 3D data.

(2) We demonstrate the feasibility of aligning different latent spaces originating from neural networks with different structures, optimization objectives, and training distributions. To make this bridging robust at extreme compression, we introduce a *Gram loss* that prevents the compressed latent from collapsing onto a few dominant directions (which we show is essential in our ablations), together with a synthetic data-generation recipe that trains the mapping networks without requiring any 3D datasets.

(3) We evaluate SQUEEZE3D for mesh, point cloud, and radiance field compression and demonstrate that generative models are a promising approach for extreme compression of 3D models. SQUEEZE3D can be flexibly extended to different encoders, generative models, and 3D formats.

2 Related Works

2.1 Neural Graphic Primitives

Neural networks are increasingly being used to represent 2D images (Sitzmann et al., 2020; Tancik et al., 2020; Gao & Jaiman, 2024), 3D objects and scenes (Sitzmann et al., 2019; Jiang et al., 2020; Peng et al., 2020; Tancik et al., 2020; Xie et al., 2022; Davies et al., 2021; Mildenhall et al., 2021; Martel et al., 2021), surface representations (Takikawa et al., 2021; Tang et al., 2023; Rakotosaona et al., 2024; Edavamadathil Sivaram et al., 2024), occupancy networks (Mescheder et al., 2019; Chen & Zhang, 2019), and signed distance fields (Michalkiewicz et al., 2019; Park et al., 2019; Atzmon & Lipman, 2020). These methods, out of the box, can also be used to compress 3D models in some format since the learned neural network weights are often already significantly smaller. Many NGP compression methods often employ standard neural network

techniques to compress MLPs by knowledge distillation (Shi & Guillemot, 2022), pruning (Isik, 2021; Xie et al., 2023; Jung et al., 2024), quantization (Shen & McClinton, 2023; Zhong et al., 2023; Yang et al., 2023; Gordon et al., 2023; Zhang et al., 2024b), factorizing tensor grids (Gao et al., 2023; Obukhov et al., 2024), low-rank approximation (Shi & Guillemot, 2022; Wang et al., 2024; Tang et al., 2022; Ji et al., 2025), and using codebooks (Li et al., 2023b;a) for quantization. Another approach is to compress feature grids or learnable embeddings (Shin & Park, 2024; Chen et al., 2024; Pham & Mandt, 2024) or extracted voxels (Wang et al., 2023; Chen et al., 2022), rather than compressing the MLP. Another set of approaches combines many of these orthogonal improvements to compressing NeRFs (Li et al., 2024). However, these methods often require training networks per scene or object, incurring significant compression latencies.

2.2 3D Autoencoders and Generators

Autoencoders encode inputs into a latent space and then decode them back into the original input space using an encoder-decoder pair; thus, they could be used as compression algorithms. Early approaches relied on volumetric representations, discretizing 3D shapes into voxel grids to leverage ConvNets for encoding and decoding (Liu et al., 2020b; Hess et al., 2023; Li et al., 2023c; Brock et al., 2016; Molnár & Tamás, 2024). While these approaches are effective for regular grid structures, these methods faced scalability challenges due to cubic memory growth with resolution increases. Subsequent advancements focused on spectral methods for encoding 3D shapes in frequency domains, offering compact latent representations but requiring precomputed basis functions that limited generalizability across shape categories (Zamorski et al., 2020; Park et al., 2019).

Several works (Zhao et al., 2023; Chen et al., 2025d; Wu et al., 2024; Lan et al., 2024) use a VAE (Kingma & Welling, 2022) to compress 3D data into a compact latent which could be used as a compressed representation. There also exist many approaches that train generators to reconstruct radiance fields (Kosiorek et al., 2021; Irshad et al., 2024; Xiang et al., 2025b), Gaussians (Wewer et al., 2024; Ma et al., 2025; Xiang et al., 2025b), or voxels (Ren et al., 2024; Xiang et al., 2025b). Some recent works also pose the problem as learning in a token-space (Chang et al., 2025; Chen et al., 2025c; Siddiqui et al., 2024; Zhang et al., 2024a; 2022; Yang et al., 2024; Luo et al., 2023; Liang & Liang, 2022; Huo et al., 2025; Marques & Da Silva Cruz, 2022; Cui et al., 2023), or with diffusion models (Zhang et al., 2025a; Liu et al., 2024; Roessle et al., 2024; Galvis et al., 2024; Ramirez-Jaime et al., 2025; Shao et al., 2024). One such generative model (Zhang et al., 2024a) is able to compress meshes with high compression ratios. A rapidly growing line of recent shape VAEs and native 3D generators learns increasingly compact latents with high-quality reconstruction (Zhang et al., 2023; Li et al., 2025a; Chen et al., 2025b; Cho et al., 2025; Li et al., 2025b; Xiang et al., 2025a; Chen et al., 2025d). Auto-decoder approaches such as ROAD (Zakharov et al., 2023) likewise encode shapes into compact codes, but require a per-shape optimization at encoding time. Compared to these methods that use autoencoders or generative models for compression, Squeeze3D does not require training specialized encoder-generators for each representation, nor any per-shape optimization at encode time. Instead, Squeeze3D aims to use existing encoders and generative models, and is in fact complementary to this line of work: any of these stronger generators can be adopted as the decoder within our framework. This enables flexibly adapting the approach as encoders and generative models evolve and supporting different 3D formats.

The work closest to our method is Generative Latent Coding (GLC) (Jia et al., 2024), which trains an autoencoder-style generative model to compress images, particularly compressing the latent representations for an image obtained through VQ-VAE (van den Oord et al., 2017). However, this method is not designed for 3D data, requires access to an encoder and decoder trained jointly, and only tests one encoder-decoder pair.

3 Method

In this work, we introduce Squeeze3D, a technique to generate highly compressed representations of 3D models by leveraging the implicit prior knowledge learnt by decoders of 3D generative models. We also leverage the availability of many 3D encoders to support an extensible set of 3D formats.

The Squeeze3D architecture is summarized in Figure 2. The key ideas of Squeeze3D are as follows. (1) We leverage existing 3D encoders to generate encoded representations for a given 3D format. Thus, the Squeeze3D architecture can be extended to support different 3D formats by using new or existing encoders.

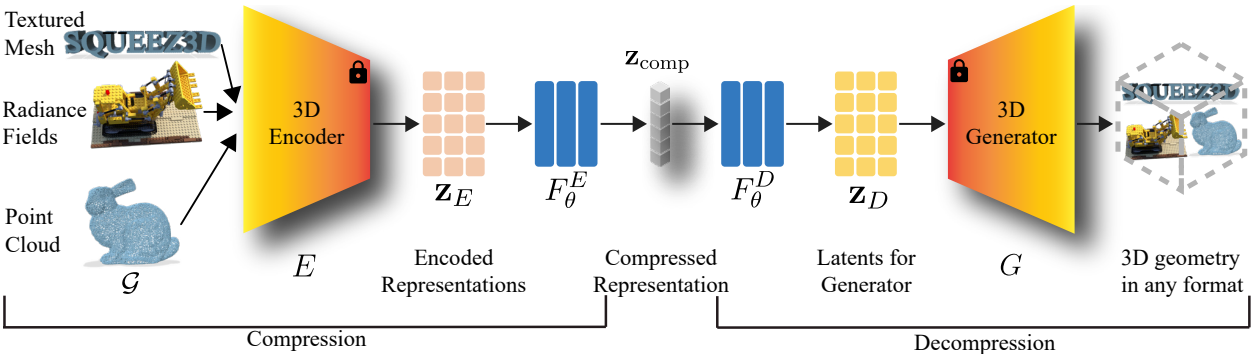


Figure 2: **Overview of our Method.** SQUEEZE3D bridges arbitrary latent spaces between 3D encoders and generators through trainable mapping networks. During compression, a 3D geometry is encoded and then transformed into a compact representation via the forward mapping network. During decompression, the reverse mapping network converts this representation into the generator's latent space, which is then used to reconstruct the original geometry.

Table 1: **Notation.** The notation we use to describe our method.

Symb.	Description	Symb.	Description
$\mathcal{G}$	A 3D geometry in some format	E	3D encoder model: $E(\mathcal{G}) \mapsto \mathbf{z}_E \in \mathbb{R}^{d_E}$
G	3D decoder model: $G(\mathbf{z}_G, c) \mapsto \mathcal{G}'$	$\mathbf{z}_E$	Latent code from the encoder: $\mathbf{z}_E \in \mathbb{R}^{d_E}$
$\mathbf{z}_G$	Latent code for the generator: $\mathbf{z}_G \in \mathbb{R}^{d_G}$	$\mathbf{z}_{\text{comp}}$	Compressed representation $\mathbf{z}_{\text{comp}} \in \mathbb{R}^{d_C}$
c	Conditioning information (*e.g.* text prompt, image) for G	F_θ^E	Forward mapping network: $F_\theta^E(\mathbf{z}_E) \mapsto \mathbf{z}_{\text{comp}}$
F_θ^D	Reverse mapping network: $F_\theta^D(\mathbf{z}_{\text{comp}}) \mapsto \mathbf{z}_G$	d_C	Dimensionality of compressed representation
d_G	Dimensionality of generator latent space	d_E	Dimensionality of encoder latent space

This approach also enables smaller mapping networks, as we now introduce. (2) We use small neural networks to convert from this encoded representation to a highly compressed latent representation (during compression) and then back into the latent space of a 3D generative model (for decompression). We refer to these neural networks as the forward and reverse mapping networks, and they effectively map between the latent space of a 3D encoder and that of a 3D generative model. Thus SQUEEZE3D can leverage a new 3D generative model by retraining the mapping networks. (3) We propose an additional loss term that enables robust training of the mapping networks to generate a highly compact latent representation that can be used to store/transmit the 3D model. We share an overview of the notation we use to describe our method in Table 1.

Mapping networks offer two major benefits over autoencoders and encoder-generator pairs, such as MeshAnything (Chen et al., 2025c): (1) the mapping networks typically provide significantly higher compression ratios than existing VAE approaches; and (2) they provide more flexibility in the choice of 3D format. For instance, InstantMesh and LRM require multi-view images as input rather than a mesh, so they cannot be used directly as 3D-to-3D autoencoders, whereas the mapping-network design lets us pair them with any 3D encoder.

3.1 Bridging Latent Spaces

SQUEEZE3D comprises two pre-trained models: (1) a 3D encoder E that maps 3D representations to a latent space, and (2) a 3D generator G that synthesizes 3D models of the same initial representation. We use the term "generator" to refer to the model whose weights and learnt priors we leverage; at decompression time we only use its *decoder* component, G, which maps a latent code to a 3D asset. For latent-diffusion generators such as LION (Zeng et al., 2022), this means we use the decoder that maps a latent to a point cloud and *bypass* the diffusion sampler entirely. Consequently, decompression is a deterministic feed-forward pass: a given compressed code always reconstructs the same 3D asset. For a given 3D representation (mesh, point

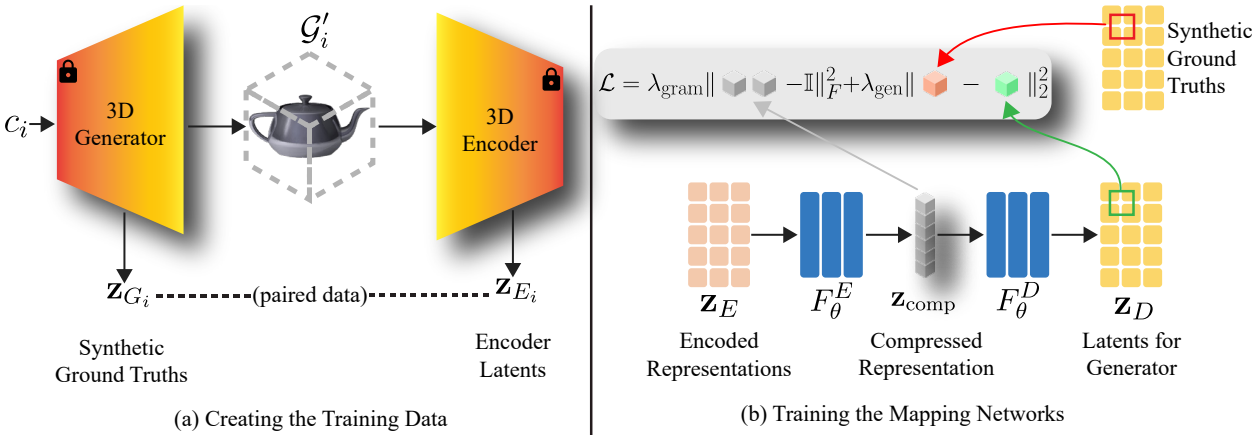


Figure 3: **Training Squeeze3D.** We show an overview of (a) our process of creating synthetic data to train the mapping networks and (b) our process of training the mapping networks.

cloud, radiance field) $\mathcal{G}$, the pre-trained encoder E produces a latent representation

$$\mathbf{z}_E = E(\mathcal{G}) \in \mathbb{R}^{d_E} \tag{1}$$

This latent $\mathbf{z}_E$ encapsulates $\mathcal{G}$, but is not in a highly compressed format. Additionally, we cannot directly use this representation with the generator G, as G operates in a different latent space. The generator G synthesizes a 3D model $\mathcal{G}'$ given a latent code $\mathbf{z}_G$ and in some cases conditioning information c, $\mathcal{G}' = G(\mathbf{z}_G, c)$. To bridge these disparate latent spaces, we train two mapping networks:

Forward Mapping Network F_θ^E: Maps from the encoder's latent space to the compressed space, $\mathbf{z}_{\text{comp}} = F_\theta^E(\mathbf{z}_E)$. **Reverse Mapping Network** F_θ^D: Maps from the compressed space to the generator's latent space, $\mathbf{z}_G = F_\theta^D(\mathbf{z}_{\text{comp}})$.

We train F_θ^E and F_θ^D together and keep the encoder E and decoder G networks frozen.

Compression. To compress any 3D model $\mathcal{G}$, the model is first encoded using the pre-trained encoder E and then mapped into a highly compressed latent $\mathbf{z}_{\text{comp}}$ using the forward mapping network F_θ^E

$$\mathbf{z}_{\text{comp}} = F_\theta^E\left(E\left(\mathcal{G}\right)\right) \tag{2}$$

Decompression. To decompress the model from its highly compressed latent representation $\mathbf{z}_{\text{comp}}$, we use the reverse mapping network F_θ^D to obtain the latent in the 3D generator space. The 3D generator then reconstructs the original 3D model $\mathcal{G}$ as $\mathcal{G}'$

$$\mathcal{G}' = G\left(F_\theta^D\left(\mathbf{z}_{\text{comp}}\right)\right) \tag{3}$$

Each encoder-generator pair and each choice of d_C requires a separately trained forward/reverse mapping pair. Once trained, that pair is reused for all objects.

3.2 Training Squeeze3D

In order to train the Squeeze3D architecture, we need to train the mapping networks for any given pair of pre-trained 3D encoders and pre-trained 3D generator models. To train these mapping networks, we need training samples from the encoder's latent space and the corresponding latents in the generator's latent space. These latents in the generator's latent space serve as "ground truth" samples during the training process. We summarize our training process in Figure 3. We now describe how to generate a training dataset with samples from both of these latent spaces.

Given a pre-trained 3D generator G' and encoder E, we first sample a diverse collection of conditioning inputs $\mathcal{C} = \{c_i\}_{i=1}^N$ appropriate for the generator model (*e.g.* text prompts for text-to-3D generators, images

for image-to-3D generators, or random noise for unconditional generators). For each conditioning input c_i, we sample a latent vector $\mathbf{z}_{G'_i}$ from the generator G' and then synthesize a 3D model using the generator: $\mathcal{G}'_i = G(\mathbf{z}_{G'_i}, c_i)$. Then we encode this synthetic or generated 3D model using the pre-trained encoder E, $\mathbf{z}_{E_i} = E(\mathcal{G}'_i)$. This methodology gives us paired synthetic data, i.e., latents, for any given pair of encoder and generator: $\{(\mathbf{z}_{E_i}, \mathbf{z}_{G'_i})\}_{i=1}^{N}$, which provides the necessary supervision for training our mapping networks.

The mapping networks F_θ^E and F_θ^D are trained together on the generated dataset using the loss shown in Equation (4).

$$\mathcal{L} = \underbrace{\lambda_{\text{gram}} \| F_\theta^E(\mathbf{z}_E) F_\theta^E(\mathbf{z}_E)^\top - \mathbb{I} \|_F^2}_{\text{orthogonality of compressed representation}} + \underbrace{\lambda_{\text{gen}} \| F_\theta^D\left(F_\theta^E(\mathbf{z}_E)\right) - \text{GT} \|_2^2}_{\text{latent-space MSE}}, \tag{4}$$

where GT represents the synthetic ground-truth latents and $\| \cdot \|_F$ denotes the Frobenius norm.

The loss function includes a *latent-space MSE* term that minimizes the difference between the generated latents and the corresponding ground-truth latents. We also add another term, which we refer to as *Gram loss*. When training SQUEEZE3D with only the latent-space MSE term, we found that the mapping networks concentrate information along a small subset of dimensions, effectively rendering many dimensions redundant.

To understand this, we empirically analyzed the latent vectors $\mathbf{z}_{\text{comp}} = F_\theta^E(\mathbf{z}_E) \in \mathbb{R}^{d_C}$ produced by our forward mapping network. For any batch of size B of encoded 3D models $\{\mathbf{z}_{E_i}\}_{i=1}^{B}$, we can compute the matrix $\mathbf{Z} \in \mathbb{R}^{B \times d_C}$ where each row is $F_\theta^E(\mathbf{z}_{E_i})$. First, we observe that if we do a singular value decomposition $\mathbf{Z} = \mathbf{U}\mathbf{\Sigma}\mathbf{V}^\top$, the singular values in $\Sigma = \text{diag}(\sigma_1, \sigma_2, \ldots, \sigma_{d_C})$ exhibit an extremely skewed distribution: $\sigma_1 \gg \sigma_2 \gg \cdots \gg \sigma_{d_C}$ where σ_i represents the i-th singular value of $\mathbf{Z}$, arranged in descending order. The condition number $\kappa = \frac{\sigma_1}{\sigma_{d_C}}$ is typically very large, indicating that the effective rank of $\mathbf{Z}$ is much lower than d_C.

Second, we observe that the correlation matrix $\mathbf{C} = \frac{1}{B}\mathbf{Z}^\top\mathbf{Z} \in \mathbb{R}^{d_C \times d_C}$ has many off-diagonal elements with large magnitudes in comparison with diagonal elements. This indicates that the dimensions of the compressed representation encode redundant information. Particularly,

$$d_{\text{eff}} = \frac{(\sum_{i=1}^{d_C} \lambda_i)^2}{\sum_{i=1}^{d_C} \lambda_i^2} \ll d_C, \tag{5}$$

where λ_i are the eigenvalues. These observations indicate that most of the information in the compressed representation was concentrated along a few dominant directions, with most dimensions contributing negligibly. For compression, this represents a severe inefficiency in utilizing the available parameter budget.

To address this, we propose the Gram loss term that is computed on the outputs of the first mapping network F_θ^E to force the outputs of F_θ^E to be orthonormal. A semi-orthogonal matrix $\mathbf{A} \in \mathbb{R}^{m \times n}$ is defined as a matrix that satisfies either $\mathbf{A}\mathbf{A}^\top = \mathbf{I}_m$ (if $m \leq n$) or $\mathbf{A}^\top\mathbf{A} = \mathbf{I}_n$ (if $n \leq m$). Our Gram loss term when minimized forces $F_\theta^E(\mathbf{z}_E) F_\theta^E(\mathbf{z}_E)^\top \approx \mathbb{I}$, which is precisely the condition for $F_\theta^E(\mathbf{z}_E)$ to be a semi-orthogonal matrix (when $d_C \leq d_E$).

4 Experiments

4.1 Experimental Setup

We train SQUEEZE3D to compress three 3D formats: textured 3D meshes, point clouds, and radiance fields, *i.e.*, grids of (rgbσ). For *3D meshes*, we train our approach with MeshAnything (Chen et al., 2025c) as the encoder and train mapping networks for three 3D generators: Shap-E (Jun & Nichol, 2023), OpenLRM (Hong et al., 2024; He & Wang, 2023), and InstantMesh (Xu et al., 2024). For *point clouds*, we train mapping networks for PointNet++ (Qi et al., 2017) as the encoder and LION (Zeng et al., 2022) as the decoder. For *radiance fields*, we train mapping networks for NeRF-MAE (Irshad et al., 2024) as both the encoder and the generator. We present additional implementation details in Section A and the mapping-network architecture in Section A.1.

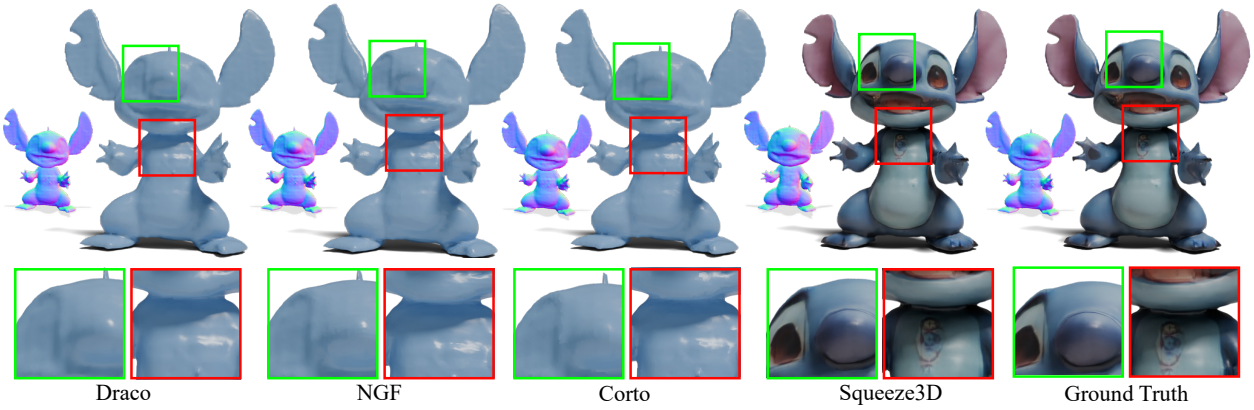


Figure 4: **Qualitative mesh compression results.** We compare SQUEEZE3D to state-of-the-art methods. Our approach maintains visually important geometric details. Additional qualitative comparisons are provided in Appendix C.4.

Training Dataset Creation. We use the method described in Section 3.2 to train SQUEEZE3D for each of our evaluated encoder-generator pairs. We now list the datasets that were used to create these latent training datasets.

Shap-E (Jun & Nichol, 2023) as the generator. We build a list of 2500 prompts using LLaMA3, each of which is used four times to build a dataset of 10,000 objects.

LRM (Hong et al., 2024; He & Wang, 2023) or InstantMesh (Xu et al., 2024) as the generator. We rendered 10,000 random objects from Objaverse (Deitke et al., 2023) which serve as image conditions. We also make sure that our rendering follows any conventions the 3D generator expects the input images to follow, for instance, white backgrounds or no backgrounds.

LION (Zeng et al., 2022) as the generator. We were able to generate plausible point clouds of 3D objects without any conditioning data from random noise.

NeRF-MAE (Irshad et al., 2024) as the generator. We generate radiance fields from the NeRF-MAE (Irshad et al., 2024) dataset.

While many other compression methods require the 3D objects to have certain properties like watertightness, we do not impose any such constraints. We emphasize that, although the mapping networks are *trained* on synthetic latents produced by the generator, they are *evaluated* entirely on standard, third-party 3D data that was not produced by our pipeline: artist-created assets from Objaverse (Deitke et al., 2023) and ShapeNet (Chang et al., 2015), real-world scanned objects from Amazon Berkeley Objects (ABO) (Appendix B.3), and captured scenes from NeRF-MAE (Irshad et al., 2024). Our reported numbers therefore measure out-of-distribution generalization to real, human-made, and scanned 3D content rather than reconstruction of the generator's own outputs. We split the datasets into training (80%) and validation (10%) sets generated from our approach. We also built a test (10%) set ($\mathcal{T}$-set) of objects from the datasets: Objaverse, ShapeNet, and NeRF-MAE, on which we report our metrics. Objaverse does not have pre-specified train and test splits. While our train and test splits are specified based on the splits used by MeshAnything (Chen et al., 2025c), we do not have access to the splits used for training the generation models. This could cause the test set we build to be a part of the training set of the generation models we use. Thus, we separately construct another test set ($\mathcal{O}$-set) of 500 3D meshes (see Section B.3) which are not in the Objaverse dataset, and report results on this test set.

Evaluation metrics. We report the standard widely used metrics, PSNR ↑, MS-SSIM ↑, and LPIPS ↓ (Zhang et al., 2018) for reconstruction quality of meshes and radiance fields. We report standard metrics, PCQM ↑ (Meynet et al., 2020), and PointSSIM ↑ (Alexiou & Ebrahimi, 2020) for reconstruction quality of point clouds. We give the precise definitions of all metrics and our rendering protocol in Section B.1. We

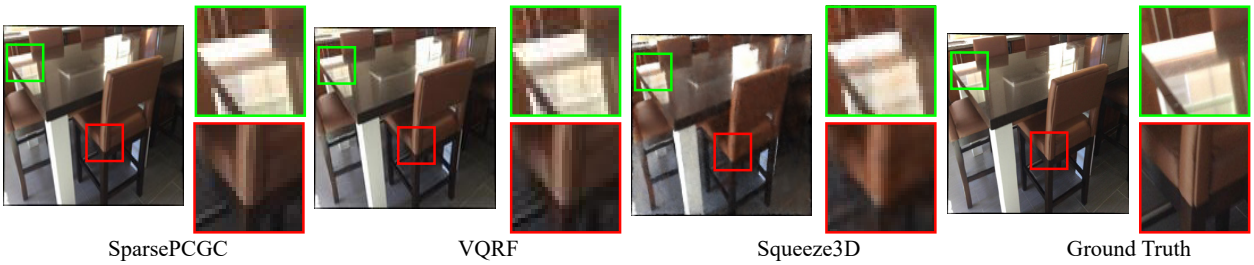


Figure 5: **Qualitative radiance field compression results.** We show qualitative results comparing Squeeze3D to state-of-the-art methods. Our approach achieves a significantly higher compression ratio while maintaining visually important geometric details.

additionally report 3D geometric distortion metrics, Chamfer Distance ↓ and EMD ↓, in Appendix C.1 and Appendix C.2 (Tables 15 and 17), and standardized bits/input-element rates in Appendix B.1 (Table 14). For all the baselines we compare against, we report average compression ratios, as well as compression and decompression times. The combined forward and reverse mapping networks range from 2.11M to 134.53M parameters (Appendix A.2, Table 9).

4.2 3D Mesh Compression

We compare Squeeze3D applied to mesh compression with existing approaches in Table 2 on our test sets. We additionally report strict 3D geometric distortion metrics (Chamfer Distance and EMD) alongside wall-clock times in Appendix C.1 (Table 15), where Squeeze3D attains a Chamfer Distance of 0.393 and an EMD of 0.0084; these complement the perceptual metrics and confirm that the decompressed geometry matches the input rather than merely looking similar in rendered views. We make the following observations.

First, Squeeze3D achieves a *mean* compression ratio of **2187** × (6.43 MB → 3 kB), more than an order of magnitude higher than that of DeepSDF (Park et al., 2019) (131 ×, 6.43 MB → 49 kB). Despite this extreme compactness, Squeeze3D preserves perceptual quality, achieving an LPIPS of 0.0274 versus 0.3704 for DeepSDF which completely fails to reconstruct complex large meshes.

Second, Squeeze3D achieves better reconstruction quality (LPIPS of 0.0274) than approaches such as Draco* (LPIPS of 0.2437), Draco† (LPIPS of 0.1039), and Corto (Lab, 2025) (LPIPS of 0.1374). Squeeze3D also achieves better quality than Neural Subdivision (Liu et al., 2020a) and DeepSDF (Park et al., 2019). Though compared to the state-of-the-art non-learned mesh compression, Squeeze3D cannot achieve as high reconstruction quality, we note that Squeeze3D achieves a significantly higher compression ratio than these approaches. Neural Geometry Fields (Edavamadathil Sivaram et al., 2024) performs better in terms of quality and compression ratios than non-learned methods but does significantly worse in terms of compression size when compared with our approach. We conclude that in achieving very high compression rates, Squeeze3D offers the highest

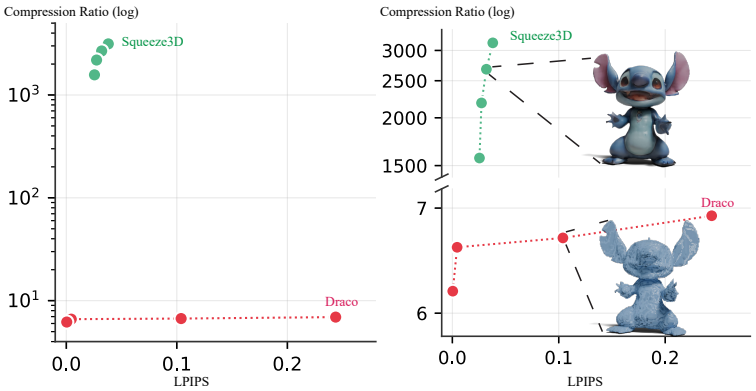


Figure 6: **Compression Ratio and Reconstruction Quality Trade-off.** We show the trade-off between compression ratio and reconstruction quality (LPIPS) for Squeeze3D and Draco. Each Squeeze3D operating point varies d_C and uses a separately trained forward/reverse mapping pair. Squeeze3D maintains high quality even at extreme compression ratios, whereas Draco's quality degrades significantly as its compression ratio increases.

Table 2: **Mesh Compression.** Quantitative comparison of SQUEEZE3D with state-of-the-art 3D mesh compression methods. We report compression ratio (CR) and quality metrics (PSNR, MS-SSIM, and LPIPS). $\mathcal{T}$ denotes our Objaverse test set, and $\mathcal{O}$ denotes the separately collected set.

Method	CR (×) (MB) ↑	$\mathcal{T}$-PSNR ↑	$\mathcal{T}$-MS-SSIM ↑	$\mathcal{T}$-LPIPS ↓	$\mathcal{O}$-PSNR ↑	$\mathcal{O}$-MS-SSIM ↑	$\mathcal{O}$-LPIPS ↓
Draco* (Galligan et al., 2018)	6.92 (6.43 / 0.93)	15.45 (±1.27)	0.7468 (±0.09)	0.2437 (±0.09)	15.40 (±1.30)	0.7450 (±0.10)	0.2450 (±0.10)
Draco† (Galligan et al., 2018)	6.70 (6.43 / 0.96)	23.33 (±1.32)	0.9576 (±0.03)	0.1039 (±0.06)	23.30 (±1.35)	0.9570 (±0.03)	0.1045 (±0.06)
Draco‡ (Galligan et al., 2018)	6.61 (6.43 / 0.97)	38.91 (±1.30)	0.9992 (±0.00)	0.0045 (±0.00)	38.89 (±1.30)	0.9991 (±0.00)	0.0046 (±0.00)
Draco§ (Galligan et al., 2018)	6.20 (6.43 / 1.04)	**48.55** (±1.54)	**1.0000** (±0.00)	**0.0004** (±0.00)	**48.50** (±1.55)	**1.0000** (±0.00)	**0.0005** (±0.00)
Corto (Lab, 2025)	45.93 (6.43 / 0.14)	20.92 (± 2.79)	0.8619 (± 0.08)	0.1374 (± 0.08)	20.85 (±2.80)	0.8610 (±0.08)	0.1380 (±0.08)
Neural Subd. (Liu et al., 2020a)	11.28 (6.43 / 0.57)	15.95 (±2.18)	0.8525 (±0.04)	0.1513 (±0.05)	15.90 (±2.20)	0.8520 (±0.04)	0.1520 (±0.05)
DeepSDF (Park et al., 2019)	131.22 (6.43 / 0.05)	8.47 (± 0.23)	0.7039 (± 0.07)	0.3704 (± 0.08)	8.21 (±0.25)	0.6850 (±0.08)	0.3912 (±0.09)
NGF (Edavamadathil Sivaram et al., 2024)	42.87 (6.43 / 0.15)	35.45 (± 3.02)	0.9987 (± 0.08)	0.0054 (± 0.03)	35.40 (±3.05)	0.9985 (±0.08)	0.0056 (±0.03)
3DShape2VecSet (Zhang et al., 2023)	342.50 (6.43 / 0.0188)	21.65 (±2.22)	0.9047 (±0.06)	0.1582 (±0.09)	21.91 (±2.55)	0.9220 (±0.04)	0.1547 (±0.07)
SQUEEZE3D (InstantMesh)	**2187.07** (6.43 / 0.003)	27.50 (±3.13)	0.9796 (±0.02)	0.0274 (±0.02)	26.95 (±3.20)	0.9905 (±0.01)	0.0124 (±0.01)

reconstruction quality. Thus, we demonstrate that leveraging 3D generative models is a promising approach for 3D compression.

While using SQUEEZE3D may not be as fast as some non-learned approaches like Draco (Galligan et al., 2018) or Corto (Lab, 2025), SQUEEZE3D is often faster than other learned methods. SQUEEZE3D is particularly much faster than training a network per object, like in NGF (Edavamadathil Sivaram et al., 2024). NGF takes on average 152638 ms to compress objects and 507 ms to decompress objects, compared to 270 ms to compress an object and 1476 ms to decompress objects for SQUEEZE3D. We qualitatively compare against Draco, Corto, and NGF for compressing meshes in Figure 4. We note that the results from our approach retain high visual quality due to the use of priors from a generative model.

4.3 Compression Ratio and Reconstruction Quality Trade-off

To better understand the trade-off between compression ratio and reconstruction quality, we analyze the performance of SQUEEZE3D against Draco (Galligan et al., 2018) across different compression settings. While many neural compression methods do not offer tunable compression ratios, SQUEEZE3D allows for different compression levels by varying the size of the compressed latent representation. Similarly, Draco offers tunable compression through its quantization parameters. In Figure 6, we plot the Pareto frontier for both methods, showing the relationship between compression ratio (x-axis) and reconstruction quality (y-axis, measured by LPIPS). We observe that Draco (Galligan et al., 2018) can only achieve compression ratios which are orders of magnitude lower than SQUEEZE3D, and as its compression ratio increases, its quality degrades significantly. In contrast, SQUEEZE3D maintains high visual quality. We further analyze the effect of the compressed-latent size on quality in Appendix C.5 (Table 18).

For applications where fine geometric details are critical, such as CAD and cultural heritage, SQUEEZE3D may be less suitable; for applications prioritizing storage or bandwidth, such as streaming and asset libraries, it offers a compelling option. We also vary d_C for point clouds and report bits per input point versus PointSSIM in Appendix C.2 (Figure 10). Each point on the SQUEEZE3D curves uses its own trained mapping pair. We do not report an analogous radiance-field sweep: increasing d_C substantially enlarges the 3D convolutional mapping networks, and training enough larger operating points was computationally infeasible in our setup. Point-cloud mapping networks are smaller, making this sweep practical. Beyond storage, mapping into the generator's *semantic* latent space yields a representation that supports operations unavailable to standard codecs such as Draco: as shown in Appendix C.1 (Figure 9), the compressed codes of two objects can be linearly interpolated to produce smooth, plausible intermediate shapes, suggesting the learnt compressed space is well-structured and could enable downstream tasks such as 3D asset mixing.

4.4 3D Point Cloud Compression

We compare our method applied to 3D point cloud compression with previous approaches in Table 3. Table 17 additionally reports strict 3D geometric distortion metrics (Chamfer Distance of 0.0285 and EMD of 0.0062). We notice that our approach achieves a significantly higher compression ratio of 58.50× (117 KB / 2.00 KB) but leads to a lower PCQM.

We demonstrate that our framework can be used off-the-shelf for point clouds but might need further improvements to match the quality of other methods. We show qualitative results in Figure 7. We note that the Draco results shown in Figure 7 correspond to a much higher-storage operating point; SQUEEZE3D's advantage lies in the extreme-compression regime, where Draco's quality degrades sharply as its ratio increases (Figure 10).

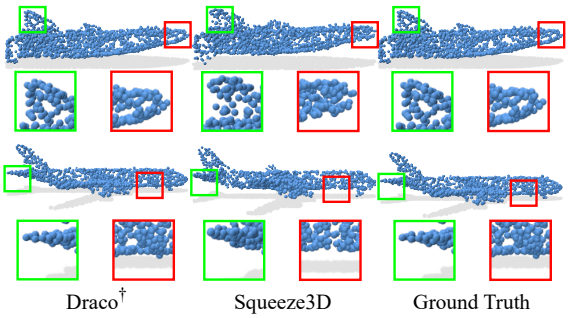


Figure 7: **Qualitative point-cloud compression.** Reconstructions from SQUEEZE3D and established codecs; quantitative results are reported in Table 3 and Fig. 10.

4.5 Radiance Field Compression

We compare SQUEEZE3D applied to radiance field compression with SparsePCGC (Wang et al., 2023) and VQRF (Li et al., 2023a) in Table 4. We choose these approaches to compare against since these works (or a setting of these works), akin to our setup, only require (rgbσ) grids. We notice that our approach achieves a significantly higher compression ratio of 619× as opposed to 40× for VQRF. SQUEEZE3D achieves these significantly higher compression rates with only a 0.0125 increase in LPIPS. We show qualitative results in Figure 5.

4.6 Comparison with Native Generative Model Encoders

We perform an additional experiment to compare SQUEEZE3D against a baseline that uses the native encoder and decoder of the generative models themselves for compression. This baseline effectively uses the latent space of the generative model as the compressed representation, and therefore serves as the closest available proxy for the quality of the "uncompressed" generator latent: it quantifies how much quality SQUEEZE3D gives up to obtain its much smaller code. (Note there is no single uncompressed latent to compare against directly, since the encoder and generator operate in different, differently sized latent spaces; see Appendix A.2, Table 10.) For reference, in the Shap-E setting (Table 5) the input mesh is encoded by MeshAnything into a 257×1024 latent, which SQUEEZE3D compresses to a 1024-dimensional code before mapping it into the Shap-E decoder latent (selected encoder and generator latent sizes are listed in Appendix A.2, Table 10). Since these generative models are designed for high-fidelity generation rather than compression, their latent spaces are typically high-dimensional.

We perform this comparison for Shap-E (Jun & Nichol, 2023), LION (Zeng et al., 2022), and NeRF-MAE (Irshad et al., 2024). We do not include InstantMesh (Xu et al., 2024) or LRM (Hong et al., 2024) in this comparison because these are feed-forward image-to-3D models that utilize 2D image encoders (e.g., DINO). They lack a native 3D-to-3D encoder that can map a 3D mesh directly to their latent space, making them unsuitable for this specific 3D compression baseline without introducing a lossy intermediate rendering step.

We report the results in Tables 5 to 7. We observe that the native baselines generally achieve high reconstruction quality (serving as an upper bound) but at significantly lower compression ratios. In contrast, SQUEEZE3D achieves orders of magnitude higher compression ratios while maintaining comparable visual

Table 3: **Point Cloud Compression.** Quantitative comparison of SQUEEZE3D with state-of-the-art point cloud compression methods. We report compression ratio (CR), compression and decompression times, and quality metrics (PCQM and PointSSIM).

Method	CR (×) (KB) ↑	Compress (ms) ↓	Decompress (ms) ↓	PCQM ↑	PointSSIM ↑
Draco‡ (Galligan et al., 2018)	15.64 (117 / 7.48)	<u>0.35</u>	<u>0.34</u>	<u>3.2875</u> (± 0.13)	**0.9722** (± 0.11)
Draco§ (Galligan et al., 2018)	22.41 (117 / 5.22)	**0.25**	**0.23**	2.1039 (± 0.08)	<u>0.9535</u> (± 0.12)
G-PCC (Schwarz et al., 2018)	37.21 (117 / 3.15)	19.76	29.92	2.8163 (± 0.10)	0.9331 (± 0.09)
V-PCC (Liu et al., 2019)	<u>50.17</u> (117 / 2.33)	2.33	234.85	**48.22** (±0.13)	0.9437 (±0.09)
SparsePCGC (Wang et al., 2023)	34.37 (117 / 3.55)	121.35	131.82	0.0653	0.1909
SQUEEZE3D (512, LION)	**58.50** (117 / 2.00)	3.85	12.74	1.8437 (±1.13)	0.4484 (±0.11)

Table 4: **Radiance Field Compression.** Quantitative comparison of SQUEEZE3D with state-of-the-art 3D radiance field compression methods. We report compression ratio (CR), compression and decompression times, and quality metrics (PSNR, MS-SSIM, and LPIPS).

Method	CR (×) (MB) ↑	Compress (ms) ↓	Decompress (ms) ↓	PSNR ↑	MS-SSIM ↑	LPIPS ↓
SparsePCGC (Wang et al., 2023)	78.92 (58.07 / 0.74)	301.39	680.82	22.26 ± 0.92	0.8947 ± 0.02	0.1400 ± 0.02
VQRF (Li et al., 2023a)	40.25 (58.07 / 1.45)	120.14	**20.58**	**29.55** ± 0.01	**0.9749** ± 0.00	**0.0618** ± 0.00
SQUEEZE3D (NeRF-MAE)	**619.41** (58.07 / 0.09)	**45.63**	75.80	26.62 ± 2.57	0.9533 ± 0.04	0.0743 ± 0.02

Table 5: **Shap-E Comparison.** Comparison between Squeeze3D (MeshAnything → Shap-E) and the native Shap-E encoder-decoder.

Method	CR (×) ↑	PSNR ↑	MS-SSIM ↑	LPIPS ↓
Shap-E Native Baseline	1.61	25.80	0.9600	0.0410
SQUEEZE3D (Shap-E)	**1607.50**	**25.92**	**0.9615**	**0.0398**

quality. In some cases, such as with Shap-E, our method can even slightly outperform the native baseline on certain metrics.

4.7 Decoder Cost and Amortization

Following standard compression conventions, our reported ratios do not include the size of the pre-trained decoder, just as a codec is not counted toward the size of each compressed file. The decoder in SQUEEZE3D is a general, object-agnostic asset, stored once and reused to decompress every object and usable for other tasks such as generation, so we do not count it toward the compressed size. We list the total decoder sizes in Table 8. These one-time costs can be amortized after hundreds of objects for meshes, tens for radiance fields, and thousands for point clouds.

5 Discussion and Limitations

The most significant limitation of our approach is its inherent dependency on the quality and expressiveness of the underlying 3D generative model. The decompressed outputs from SQUEEZE3D fundamentally cannot exceed the quality of what the generator can produce, as the generator serves as both a prior knowledge base and a quality ceiling. In our evaluation, we observed that reconstruction fidelity is directly correlated with the generative capabilities of the chosen generator model.

For instance, when using the Shap-E (Jun & Nichol, 2023) generator, we found it challenging to faithfully reproduce highly complex objects due to limitations in the model's semantic capacity (see Section C.6). Concretely, geometric detail that lies beyond the generator's representational capacity, such as fine threads on a screw or small embossed text, is smoothed away or hallucinated rather than reconstructed faithfully (Section C.6); the generator acts as a hard quality ceiling. This limitation, however, positions SQUEEZE3D to benefit automatically from future advancements in 3D generative modeling. Newer generators such as Hunyuan3D-2.5 (Lai et al., 2025) and TRELLIS (Xiang et al., 2025b;a) may provide broader priors and higher-fidelity reconstruction. Their larger latent spaces may require wider mapping networks and additional compute.

Table 8: Storage size of each decoder used at decompression.

Decoder	Total size
SQUEEZE3D	
Shap-E	905 MB
InstantMesh	1.51 GB
OpenLRM	1.04 GB
LION	270 MB
NeRF-MAE	306 MB
Baselines	
3DShape2VecSet	389 MB
DeepSDF	7.4 MB

Table 6: **LION Comparison.** Comparison between SQUEEZE3D (PointNet++ → LION) and the native LION encoder-decoder.

Method	CR (×) ↑	PCQM ↑	PointSSIM ↑	Chamfer ↓
LION Native Baseline	<u>3.60</u>	**2.1000**	**0.5100**	**0.0210**
SQUEEZE3D (LION)	**58.50**	<u>1.8437</u>	<u>0.4484</u>	<u>0.0285</u>

Table 7: **NeRF-MAE Comparison.** Comparison between SQUEEZE3D (NeRF-MAE → NeRF-MAE) and the native NeRF-MAE encoder-decoder.

Method	CR (×) ↑	PSNR ↑	MS-SSIM ↑	LPIPS ↓
NeRF-MAE Native Baseline	<u>7.44</u>	**28.10**	**0.9700**	**0.0550**
SQUEEZE3D (NeRF-MAE)	**619.41**	<u>26.62</u>	<u>0.9533</u>	<u>0.0743</u>

Since SQUEEZE3D is designed as a compression-decompression framework that should not require per-scene retraining, the generalization capability of our mapping networks to unseen 3D models is crucial. We evaluated this aspect by testing on a dataset of 500 3D meshes and 227 radiance fields, which served as out-of-distribution samples, and found that our approach maintains consistent performance (see Section C). Nevertheless, for certain outlier cases where the input 3D model contains features far from the distribution seen during training, compression quality may degrade. Encoder-limited failures may benefit from multiscale encoders (Dagli et al., 2026) or higher-resolution input sampling, while generator-limited failures require a broader prior or a conventional fallback codec. A practical deployment could use the native encoder's reconstruction error or an OOD detector to identify risky inputs and route them to a standard codec.

6 Conclusion

In this work, we answer: *How can we bridge the latent spaces of different models?* We do so with losses in the latent space, without any reconstruction-based losses. As an application, we apply this to 3D. We introduce SQUEEZE3D, a framework for 3D compression that leverages the rich priors in existing 3D generation models, bridging arbitrary latent spaces between different models to enable extreme compression ratios while maintaining high visual fidelity. By mapping between latent spaces, we avoid the per-scene optimization that plagues many neural compression methods, yielding faster compression and decompression than learned approaches that train a network per object (*e.g.*, NGF), at competitive visual quality, though the wall-clock time remains dominated by the chosen encoder and decoder. We hope this work inspires more research on using generative models for compressing 3D data.

Broader Impact Statement

Compression with generative priors can reconstruct geometry that is perceptually plausible but not faithful to the original: fine details, text, and structures outside the generator's prior may be smoothed, altered, or hallucinated. Consequently, SQUEEZE3D should not be used where exact geometry is safety-critical without fidelity checks and a fallback to a conventional codec or the original asset.

Acknowledgements

Resources used in preparing this research were provided in part by the Province of Ontario, the Government of Canada through CIFAR, and companies sponsoring the Vector Institute.

References

Evangelos Alexiou and Touradj Ebrahimi. Towards a point cloud structural similarity metric. In *2020 IEEE International Conference on Multimedia & Expo Workshops (ICMEW)*, pp. 1–6, 2020. doi: 10.1109/ICMEW46912.2020.9106005.

Matan Atzmon and Yaron Lipman. Sal: Sign agnostic learning of shapes from raw data. In *Proceedings of the IEEE/CVF conference on computer vision and pattern recognition*, pp. 2565–2574, 2020.

Jimmy Lei Ba, Jamie Ryan Kiros, and Geoffrey E. Hinton. Layer normalization, 2016. URL `https://arxiv.org/abs/1607.06450`.

Andrew Brock, Theodore Lim, J. M. Ritchie, and Nick Weston. Generative and discriminative voxel modeling with convolutional neural networks, 2016. URL `https://arxiv.org/abs/1608.04236`.

Edwin Catmull and James Clark. Recursively generated b-spline surfaces on arbitrary topological meshes. In *Seminal graphics: pioneering efforts that shaped the field*, pp. 183–188. 1998.

Angel X. Chang, Thomas Funkhouser, Leonidas Guibas, Pat Hanrahan, Qixing Huang, Zimo Li, Silvio Savarese, Manolis Savva, Shuran Song, Hao Su, Jianxiong Xiao, Li Yi, and Fisher Yu. Shapenet: An information-rich 3d model repository, 2015. URL `https://arxiv.org/abs/1512.03012`.

Jen-Hao Rick Chang, Yuyang Wang, Miguel Angel Bautista Martin, Jiatao Gu, Xiaoming Zhao, Josh Susskind, and Oncel Tuzel. 3d shape tokenization via latent flow matching, 2025. URL `https://arxiv.org/abs/2412.15618`.

Anpei Chen, Zexiang Xu, Andreas Geiger, Jingyi Yu, and Hao Su. Tensorf: Tensorial radiance fields. In *European conference on computer vision*, pp. 333–350. Springer, 2022.

Junyu Chen, Han Cai, Junsong Chen, Enze Xie, Shang Yang, Haotian Tang, Muyang Li, and Song Han. Deep compression autoencoder for efficient high-resolution diffusion models. In *The Thirteenth International Conference on Learning Representations*, 2025a. URL `https://openreview.net/forum?id=wH8XXUOUZU`.

Rui Chen, Jianfeng Zhang, Yixun Liang, Guan Luo, Weiyu Li, Jiarui Liu, Xiu Li, Xiaoxiao Long, Jiashi Feng, and Ping Tan. Dora: Sampling and benchmarking for 3d shape variational auto-encoders. In *Proceedings of the IEEE/CVF Conference on Computer Vision and Pattern Recognition (CVPR)*, pp. 16251–16261, June 2025b.

Yihang Chen, Qianyi Wu, Mehrtash Harandi, and Jianfei Cai. How far can we compress instant-ngp-based nerf? In *Proceedings of the IEEE/CVF Conference on Computer Vision and Pattern Recognition (CVPR)*, pp. 20321–20330, June 2024.

Yiwen Chen, Tong He, Di Huang, Weicai Ye, Sijin Chen, Jiaxiang Tang, Zhongang Cai, Lei Yang, Gang Yu, Guosheng Lin, and Chi Zhang. Meshanything: Artist-created mesh generation with autoregressive transformers. In *The Thirteenth International Conference on Learning Representations*, 2025c. URL `https://openreview.net/forum?id=KGZAs8VcOM`.

Zhaoxi Chen, Jiaxiang Tang, Yuhao Dong, Ziang Cao, Fangzhou Hong, Yushi Lan, Tengfei Wang, Haozhe Xie, Tong Wu, Shunsuke Saito, Liang Pan, Dahua Lin, and Ziwei Liu. 3dtopia-xl: Scaling high-quality 3d asset generation via primitive diffusion. In *Proceedings of the IEEE/CVF Conference on Computer Vision and Pattern Recognition (CVPR)*, pp. 26576–26586, June 2025d.

Zhiqin Chen and Hao Zhang. Learning implicit fields for generative shape modeling. In *Proceedings of the IEEE/CVF conference on computer vision and pattern recognition*, pp. 5939–5948, 2019.

In Cho, Youngbeom Yoo, Subin Jeon, and Seon Joo Kim. Representing 3d shapes with 64 latent vectors for 3d diffusion models. In *Proceedings of the IEEE/CVF International Conference on Computer Vision (ICCV)*, pp. 28556–28566, October 2025.

Jonathan Cohen, Marc Olano, and Dinesh Manocha. Appearance-preserving simplification. In *Proceedings of the 25th annual conference on Computer graphics and interactive techniques*, pp. 115–122, 1998.

Jasmine Collins, Shubham Goel, Kenan Deng, Achleshwar Luthra, Leon Xu, Erhan Gundogdu, Xi Zhang, Tomas F Yago Vicente, Thomas Dideriksen, Himanshu Arora, Matthieu Guillaumin, and Jitendra Malik. Abo: Dataset and benchmarks for real-world 3d object understanding. *CVPR*, 2022.

Mingyue Cui, Junhua Long, Mingjian Feng, Boyang Li, and Huang Kai. Octformer: Efficient octree-based transformer for point cloud compression with local enhancement. *Proceedings of the AAAI Conference on Artificial Intelligence*, 37(1):470–478, Jun. 2023. doi: 10.1609/aaai.v37i1.25121. URL https://ojs.aaai.org/index.php/AAAI/article/view/25121.

Ruikai Cui, Weizhe Liu, Weixuan Sun, Senbo Wang, Taizhang Shang, Yang Li, Xibin Song, Han Yan, Zhennan Wu, Shenzhou Chen, Hongdong Li, and Pan Ji. Neusdfusion: A spatial-aware generative model for 3d shape completion, reconstruction, and generation. In Aleš Leonardis, Elisa Ricci, Stefan Roth, Olga Russakovsky, Torsten Sattler, and Gül Varol (eds.), *Computer Vision – ECCV 2024*, pp. 1–18, Cham, 2025. Springer Nature Switzerland. ISBN 978-3-031-72655-2.

Rishit Dagli, Donglai Xiang, Vismay Modi, Xuning Yang, Gavriel State, David I.W. Levin, and Maria Shugrina. Adaptive volumetric mechanical property fields invariant to resolution. In *Forty-third International Conference on Machine Learning*, 2026.

Thomas Davies, Derek Nowrouzezahrai, and Alec Jacobson. On the effectiveness of weight-encoded neural implicit 3d shapes, 2021. URL https://arxiv.org/abs/2009.09808.

Michael Deering. Geometry compression. In *Proceedings of the 22nd Annual Conference on Computer Graphics and Interactive Techniques*, SIGGRAPH '95, pp. 13–20, New York, NY, USA, 1995. Association for Computing Machinery. ISBN 0897917014. doi: 10.1145/218380.218391. URL https://doi.org/10.1145/218380.218391.

Matt Deitke, Ruoshi Liu, Matthew Wallingford, Huong Ngo, Oscar Michel, Aditya Kusupati, Alan Fan, Christian Laforte, Vikram Voleti, Samir Yitzhak Gadre, Eli VanderBilt, Aniruddha Kembhavi, Carl Vondrick, Georgia Gkioxari, Kiana Ehsani, Ludwig Schmidt, and Ali Farhadi. Objaverse-XL: A universe of 10m+ 3d objects. In *Thirty-seventh Conference on Neural Information Processing Systems Datasets and Benchmarks Track*, 2023. URL https://openreview.net/forum?id=Sq3CLKJeiz.

Alexey Dosovitskiy, Lucas Beyer, Alexander Kolesnikov, Dirk Weissenborn, Xiaohua Zhai, Thomas Unterthiner, Mostafa Dehghani, Matthias Minderer, Georg Heigold, Sylvain Gelly, Jakob Uszkoreit, and Neil Houlsby. An image is worth 16x16 words: Transformers for image recognition at scale. In *International Conference on Learning Representations*, 2021. URL https://openreview.net/forum?id=YicbFdNTTy.

Venkataram Edavamadathil Sivaram, Tzu-Mao Li, and Ravi Ramamoorthi. Neural geometry fields for meshes. In *ACM SIGGRAPH 2024 Conference Papers*, SIGGRAPH '24, New York, NY, USA, 2024. Association for Computing Machinery. ISBN 9798400705250. doi: 10.1145/3641519.3657399. URL https://doi.org/10.1145/3641519.3657399.

Zhiwen Fan, Kevin Wang, Kairun Wen, Zehao Zhu, Dejia Xu, and Zhangyang Wang. Lightgaussian: unbounded 3d gaussian compression with 15x reduction and 200+ fps. In *Proceedings of the 38th International Conference on Neural Information Processing Systems*, NIPS '24, Red Hook, NY, USA, 2024. Curran Associates Inc. ISBN 9798331314385.

Frank Galligan, Michael Hemmer, Ondrej Stava, Fan Zhang, and Jamieson Brettle. Google/draco: a library for compressing and decompressing 3d geometric meshes and point clouds, 2018.

Juan D. Galvis, Xingxing Zuo, Simon Schaefer, and Stefan Leutengger. Sc-diff: 3d shape completion with latent diffusion models, 2024. URL https://arxiv.org/abs/2403.12470.

Quankai Gao, Qiangeng Xu, Hao Su, Ulrich Neumann, and Zexiang Xu. Strivec: Sparse tri-vector radiance fields. In *Proceedings of the IEEE/CVF International Conference on Computer Vision (ICCV)*, pp. 17569–17579, October 2023.

Rui Gao and Rajeev K. Jaiman. H-siren: Improving implicit neural representations with hyperbolic periodic functions, 2024. URL https://arxiv.org/abs/2410.04716.

Michael Garland and Paul S. Heckbert. Surface simplification using quadric error metrics. In *Proceedings of the 24th Annual Conference on Computer Graphics and Interactive Techniques*, SIGGRAPH '97, pp. 209–216, USA, 1997. ACM Press/Addison-Wesley Publishing Co. ISBN 0897918967. doi: 10.1145/258734.258849. URL https://doi.org/10.1145/258734.258849.

Cameron Gordon, Shin-Fang Chng, Lachlan MacDonald, and Simon Lucey. On quantizing implicit neural representations. In *Proceedings of the IEEE/CVF Winter Conference on Applications of Computer Vision*, pp. 341–350, 2023.

Sara Hahner and Jochen Garcke. Mesh convolutional autoencoder for semi-regular meshes of different sizes. In *Proceedings of the IEEE/CVF Winter Conference on Applications of Computer Vision (WACV)*, pp. 885–894, January 2022.

Kaiming He, Xiangyu Zhang, Shaoqing Ren, and Jian Sun. Identity mappings in deep residual networks. In Bastian Leibe, Jiri Matas, Nicu Sebe, and Max Welling (eds.), *Computer Vision – ECCV 2016*, pp. 630–645, Cham, 2016. Springer International Publishing. ISBN 978-3-319-46493-0.

Zexin He and Tengfei Wang. Openlrm: Open-source large reconstruction models. https://github.com/3DTopia/OpenLRM, 2023.

Dan Hendrycks and Kevin Gimpel. Gaussian error linear units (gelus), 2023. URL https://arxiv.org/abs/1606.08415.

Amir Hertz, Rana Hanocka, Raja Giryes, and Daniel Cohen-Or. Deep geometric texture synthesis. *ACM Trans. Graph.*, 39(4), August 2020. ISSN 0730-0301. doi: 10.1145/3386569.3392471. URL https://doi.org/10.1145/3386569.3392471.

Georg Hess, Johan Jaxing, Elias Svensson, David Hagerman, Christoffer Petersson, and Lennart Svensson. Masked autoencoder for self-supervised pre-training on lidar point clouds. In *2023 IEEE/CVF Winter Conference on Applications of Computer Vision Workshops (WACVW)*, pp. 350–359. IEEE, January 2023. doi: 10.1109/wacvw58289.2023.00039. URL http://dx.doi.org/10.1109/WACVW58289.2023.00039.

Yicong Hong, Kai Zhang, Jiuxiang Gu, Sai Bi, Yang Zhou, Difan Liu, Feng Liu, Kalyan Sunkavalli, Trung Bui, and Hao Tan. LRM: Large reconstruction model for single image to 3d. In *The Twelfth International Conference on Learning Representations*, 2024. URL https://openreview.net/forum?id=sllU8vvsFF.

Hugues Hoppe, Tony DeRose, Tom Duchamp, Mark Halstead, Hubert Jin, John McDonald, Jean Schweitzer, and Werner Stuetzle. Piecewise smooth surface reconstruction. In *Proceedings of the 21st annual conference on Computer graphics and interactive techniques*, pp. 295–302, 1994.

Xiao Huo, Junhui Hou, Shuai Wan, and Fuzheng Yang. Rendering-oriented 3d point cloud attribute compression using sparse tensor-based transformer. *IEEE Transactions on Circuits and Systems for Video Technology*, 35(8):8283–8298, 2025. doi: 10.1109/TCSVT.2025.3546626.

Muhammad Zubair Irshad, Sergey Zakharov, Vitor Guizilini, Adrien Gaidon, Zsolt Kira, and Rares Ambrus. Nerf-mae: Masked autoencoders for self-supervised 3d representation learning for neural radiance fields. In *European Conference on Computer Vision*, pp. 434–453. Springer, 2024.

Berivan Isik. Neural 3d scene compression via model compression. *arXiv preprint arXiv:2105.03120*, 2021.

Yiping Ji, Hemanth Saratchandran, Cameron Gordon, Zeyu Zhang, and Simon Lucey. Efficient learning with sine-activated low-rank matrices. In *The Thirteenth International Conference on Learning Representations*, 2025. URL https://openreview.net/forum?id=cWGCkd7mCp.

Zhaoyang Jia, Jiahao Li, Bin Li, Houqiang Li, and Yan Lu. Generative latent coding for ultra-low bitrate image compression. In *2024 IEEE/CVF Conference on Computer Vision and Pattern Recognition (CVPR)*, pp. 26088–26098, 2024. doi: 10.1109/CVPR52733.2024.02465.

Chiyu Jiang, Avneesh Sud, Ameesh Makadia, Jingwei Huang, Matthias Nießner, Thomas Funkhouser, et al. Local implicit grid representations for 3d scenes. In *Proceedings of the IEEE/CVF Conference on Computer Vision and Pattern Recognition*, pp. 6001–6010, 2020.

Heewoo Jun and Alex Nichol. Shap-e: Generating conditional 3d implicit functions, 2023. URL `https://arxiv.org/abs/2305.02463`.

Yeonsung Jung, Heecheol Yun, Joonhyung Park, Jin-Hwa Kim, and Eunho Yang. PruNeRF: Segment-centric dataset pruning via 3D spatial consistency. In Ruslan Salakhutdinov, Zico Kolter, Katherine Heller, Adrian Weller, Nuria Oliver, Jonathan Scarlett, and Felix Berkenkamp (eds.), *Proceedings of the 41st International Conference on Machine Learning*, volume 235 of *Proceedings of Machine Learning Research*, pp. 22696–22709. PMLR, 21–27 Jul 2024. URL `https://proceedings.mlr.press/v235/jung24b.html`.

Bernhard Kerbl, Georgios Kopanas, Thomas Leimkühler, and George Drettakis. 3d gaussian splatting for real-time radiance field rendering. *ACM Transactions on Graphics*, 42(4), July 2023. URL `https://repo-sam.inria.fr/fungraph/3d-gaussian-splatting/`.

Diederik P Kingma and Max Welling. Auto-encoding variational bayes. 2022. URL `https://arxiv.org/abs/1312.6114`.

Adam R Kosiorek, Heiko Strathmann, Daniel Zoran, Pol Moreno, Rosalia Schneider, Sona Mokrá, and Danilo Jimenez Rezende. Nerf-vae: A geometry aware 3d scene generative model. In *International Conference on Machine Learning*, pp. 5742–5752. PMLR, 2021.

Visual Computing Lab. Corto: Mesh compression library. `https://github.com/cnr-isti-vclab/corto`, 2025. Accessed: March 03, 2025.

Zeqiang Lai, Yunfei Zhao, Haolin Liu, Zibo Zhao, Qingxiang Lin, Huiwen Shi, Xianghui Yang, Mingxin Yang, Shuhui Yang, Yifei Feng, Sheng Zhang, Xin Huang, Di Luo, Fan Yang, Fang Yang, Lifu Wang, Sicong Liu, Yixuan Tang, Yulin Cai, Zebin He, Tian Liu, Yuhong Liu, Jie Jiang, Linus, Jingwei Huang, and Chunchao Guo. Hunyuan3d 2.5: Towards high-fidelity 3d assets generation with ultimate details, 2025. URL `https://arxiv.org/abs/2506.16504`.

Yushi Lan, Fangzhou Hong, Shuai Yang, Shangchen Zhou, Xuyi Meng, Bo Dai, Xingang Pan, and Chen Change Loy. Ln3diff: Scalable latent neural fields diffusion for speedy 3d generation. In *European Conference on Computer Vision*, pp. 112–130. Springer, 2024.

Joo Chan Lee, Daniel Rho, Xiangyu Sun, Jong Hwan Ko, and Eunbyung Park. Compact 3d gaussian representation for radiance field. In *Proceedings of the IEEE/CVF Conference on Computer Vision and Pattern Recognition (CVPR)*, pp. 21719–21728, June 2024.

Thibault Lescoat, Hsueh-Ti Derek Liu, Jean-Marc Thiery, Alec Jacobson, Tamy Boubekeur, and Maks Ovsjanikov. Spectral mesh simplification. *Computer Graphics Forum*, 39(2):315–324, 2020. doi: https://doi.org/10.1111/cgf.13932. URL `https://onlinelibrary.wiley.com/doi/abs/10.1111/cgf.13932`.

Lingzhi Li, Zhen Shen, Zhongshu Wang, Li Shen, and Liefeng Bo. Compressing volumetric radiance fields to 1 mb. In *2023 IEEE/CVF Conference on Computer Vision and Pattern Recognition (CVPR)*, pp. 4222–4231, 2023a. doi: 10.1109/CVPR52729.2023.00411.

Lingzhi Li, Zhongshu Wang, Zhen Shen, Li Shen, and Ping Tan. Compact real-time radiance fields with neural codebook. In *2023 IEEE International Conference on Multimedia and Expo (ICME)*, pp. 2189–2194. IEEE, 2023b.

Sicheng Li, Hao Li, Yiyi Liao, and Lu Yu. Nerfcodec: Neural feature compression meets neural radiance fields for memory-efficient scene representation. In *Proceedings of the IEEE/CVF Conference on Computer Vision and Pattern Recognition (CVPR)*, pp. 21274–21283, June 2024.

Wei Li, Yufei Chen, Zhicheng Wang, Weidong Zhao, and Lin Chen. An improved decimation of triangle meshes based on curvature. In Duoqian Miao, Witold Pedrycz, Dominik Ślezak, Georg Peters, Qinghua Hu, and Ruizhi Wang (eds.), *Rough Sets and Knowledge Technology*, pp. 260–271, Cham, 2014. Springer International Publishing. ISBN 978-3-319-11740-9.

Weiyu Li, Jiarui Liu, Hongyu Yan, Rui Chen, Yixun Liang, Xuelin Chen, Ping Tan, and Xiaoxiao Long. Craftsman3d: High-fidelity mesh generation with 3d native diffusion and interactive geometry refiner. In *Proceedings of the IEEE/CVF Conference on Computer Vision and Pattern Recognition (CVPR)*, pp. 5307–5317, June 2025a.

Yangguang Li, Zi-Xin Zou, Zexiang Liu, Dehu Wang, Yuan Liang, Zhipeng Yu, Xingchao Liu, Yuan-Chen Guo, Ding Liang, Wanli Ouyang, and Yan-Pei Cao. Triposg: High-fidelity 3d shape synthesis using large-scale rectified flow models. *IEEE Transactions on Pattern Analysis and Machine Intelligence*, pp. 1–18, 2025b. doi: 10.1109/TPAMI.2025.3633512.

Yiming Li, Zhiding Yu, Christopher Choy, Chaowei Xiao, Jose M. Alvarez, Sanja Fidler, Chen Feng, and Anima Anandkumar. Voxformer: Sparse voxel transformer for camera-based 3d semantic scene completion. In *2023 IEEE/CVF Conference on Computer Vision and Pattern Recognition (CVPR)*, pp. 9087–9098, 2023c. doi: 10.1109/CVPR52729.2023.00877.

Zujie Liang and Fan Liang. Transpcc: Towards deep point cloud compression via transformers. In *Proceedings of the 2022 International Conference on Multimedia Retrieval*, ICMR '22, pp. 1–5, New York, NY, USA, 2022. Association for Computing Machinery. ISBN 9781450392389. doi: 10.1145/3512527.3531423. URL https://doi.org/10.1145/3512527.3531423.

Hao Liu, Hui Yuan, Qi Liu, Junhui Hou, and Ju Liu. A comprehensive study and comparison of core technologies for mpeg 3-d point cloud compression. *IEEE Transactions on Broadcasting*, 66(3):701–717, 2019.

Hsueh-Ti Derek Liu, Vladimir G. Kim, Siddhartha Chaudhuri, Noam Aigerman, and Alec Jacobson. Neural subdivision. *ACM Trans. Graph.*, 39(4), August 2020a. ISSN 0730-0301. doi: 10.1145/3386569.3392418. URL https://doi.org/10.1145/3386569.3392418.

Juncheng Liu, Steven Mills, and Brendan McCane. Variational autoencoder for 3d voxel compression. In *2020 35th International Conference on Image and Vision Computing New Zealand (IVCNZ)*, pp. 1–6, 2020b. doi: 10.1109/IVCNZ51579.2020.9290656.

Kai Liu, Kang You, and Pan Gao. Diff-pcc: Diffusion-based neural compression for 3d point clouds, 2024. URL https://arxiv.org/abs/2408.10543.

Charles Loop. Smooth subdivision surfaces based on triangles. 1987.

Zhe Luo, Wenjing Jia, and Stuart W. Perry. Transformer-based geometric point cloud compression with local neighbor aggregation. In *DICTA*, pp. 223–228, 2023. URL https://doi.org/10.1109/DICTA60407.2023.00038.

Qi Ma, Yue Li, Bin Ren, Nicu Sebe, Ender Konukoglu, Theo Gevers, Luc Van Gool, and Danda Pani Paudel. A large-scale dataset of gaussian splats and their self-supervised pretraining. In *International Conference on 3D Vision 2025*, 2025. URL https://openreview.net/forum?id=rXlpYdCExk.

Miguel Marques and Luís A. Da Silva Cruz. Explorations on 3d point clouds coding using transformers and patches. In *2022 10th European Workshop on Visual Information Processing (EUVIP)*, pp. 1–6, 2022. doi: 10.1109/EUVIP53989.2022.9922700.

Julien N. P. Martel, David B. Lindell, Connor Z. Lin, Eric R. Chan, Marco Monteiro, and Gordon Wetzstein. Acorn: adaptive coordinate networks for neural scene representation. *ACM Trans. Graph.*, 40(4), July 2021. ISSN 0730-0301. doi: 10.1145/3450626.3459785. URL https://doi.org/10.1145/3450626.3459785.

Lars Mescheder, Michael Oechsle, Michael Niemeyer, Sebastian Nowozin, and Andreas Geiger. Occupancy networks: Learning 3d reconstruction in function space. In *Proceedings of the IEEE/CVF conference on computer vision and pattern recognition*, pp. 4460–4470, 2019.

Gabriel Meynet, Yana Nehmé, Julie Digne, and Guillaume Lavoué. Pcqm: A full-reference quality metric for colored 3d point clouds. In *2020 Twelfth International Conference on Quality of Multimedia Experience (QoMEX)*, pp. 1–6, 2020. doi: 10.1109/QoMEX48832.2020.9123147.

Mateusz Michalkiewicz, Jhony K Pontes, Dominic Jack, Mahsa Baktashmotlagh, and Anders Eriksson. Implicit surface representations as layers in neural networks. In *Proceedings of the IEEE/CVF International Conference on Computer Vision*, pp. 4743–4752, 2019.

Ben Mildenhall, Pratul P. Srinivasan, Matthew Tancik, Jonathan T. Barron, Ravi Ramamoorthi, and Ren Ng. Nerf: representing scenes as neural radiance fields for view synthesis. *Commun. ACM*, 65(1):99–106, December 2021. ISSN 0001-0782. doi: 10.1145/3503250. URL https://doi.org/10.1145/3503250.

Szilárd Molnár and Levente Tamás. Variational autoencoders for 3d data processing. *Artificial Intelligence Review*, 57(2):42, 2024.

Thomas Müller, Alex Evans, Christoph Schied, and Alexander Keller. Instant neural graphics primitives with a multiresolution hash encoding. *ACM Transactions on Graphics*, 41(4):1–15, July 2022. ISSN 1557-7368. doi: 10.1145/3528223.3530127. URL http://dx.doi.org/10.1145/3528223.3530127.

Anton Obukhov, Mikhail Usvyatsov, Christos Sakaridis, Konrad Schindler, and Luc Van Gool. Tt-nf: Tensor train neural fields. *IEEE Journal of Selected Topics in Signal Processing*, 18(6):1024–1035, 2024. doi: 10.1109/JSTSP.2024.3454980.

Jeong Joon Park, Peter Florence, Julian Straub, Richard Newcombe, and Steven Lovegrove. Deepsdf: Learning continuous signed distance functions for shape representation. In *Proceedings of the IEEE/CVF conference on computer vision and pattern recognition*, pp. 165–174, 2019.

Songyou Peng, Michael Niemeyer, Lars Mescheder, Marc Pollefeys, and Andreas Geiger. Convolutional occupancy networks. In *Computer Vision–ECCV 2020: 16th European Conference, Glasgow, UK, August 23–28, 2020, Proceedings, Part III 16*, pp. 523–540. Springer, 2020.

Tuan Pham and Stephan Mandt. Neural NeRF compression. In Ruslan Salakhutdinov, Zico Kolter, Katherine Heller, Adrian Weller, Nuria Oliver, Jonathan Scarlett, and Felix Berkenkamp (eds.), *Proceedings of the 41st International Conference on Machine Learning*, volume 235 of *Proceedings of Machine Learning Research*, pp. 40592–40610. PMLR, 21–27 Jul 2024. URL https://proceedings.mlr.press/v235/pham24a.html.

Rolandos Alexandros Potamias, Stylianos Ploumpis, and Stefanos Zafeiriou. Neural mesh simplification. In *Proceedings of the IEEE/CVF Conference on Computer Vision and Pattern Recognition*, pp. 18583–18592, 2022.

Charles Ruizhongtai Qi, Li Yi, Hao Su, and Leonidas J Guibas. Pointnet++: Deep hierarchical feature learning on point sets in a metric space. In I. Guyon, U. Von Luxburg, S. Bengio, H. Wallach, R. Fergus, S. Vishwanathan, and R. Garnett (eds.), *Advances in Neural Information Processing Systems*, volume 30. Curran Associates, Inc., 2017. URL https://proceedings.neurips.cc/paper_files/paper/2017/file/d8bf84be3800d12f74d8b05e9b89836f-Paper.pdf.

Marie-Julie Rakotosaona, Fabian Manhardt, Diego Martin Arroyo, Michael Niemeyer, Abhijit Kundu, and Federico Tombari. Nerfmeshing: Distilling neural radiance fields into geometrically-accurate 3d meshes. In *2024 International Conference on 3D Vision (3DV)*, pp. 1156–1165, 2024. doi: 10.1109/3DV62453.2024.00093.

Andres Ramirez-Jaime, Gonzalo R. Arce, Nestor Porras-Diaz, Oleg Ieremeiev, Andrii Rubel, Vladimir Lukin, Mateusz Kopytek, Piotr Lech, Jarosław Fastowicz, and Krzysztof Okarma. Generative diffusion models for compressed sensing of satellite lidar data: Evaluating image quality metrics in forest landscape reconstruction. *Remote Sensing*, 17(7), 2025. ISSN 2072-4292. doi: 10.3390/rs17071215. URL https://www.mdpi.com/2072-4292/17/7/1215.

Xuanchi Ren, Jiahui Huang, Xiaohui Zeng, Ken Museth, Sanja Fidler, and Francis Williams. Xcube: Large-scale 3d generative modeling using sparse voxel hierarchies. In *Proceedings of the IEEE/CVF Conference on Computer Vision and Pattern Recognition*, 2024.

Barbara Roessle, Norman Müller, Lorenzo Porzi, Samuel Rota Bulò, Peter Kontschieder, Angela Dai, and Matthias Nießner. L3dg: Latent 3d gaussian diffusion. In *SIGGRAPH Asia 2024 Conference Papers*, December 2024.

Olaf Ronneberger, Philipp Fischer, and Thomas Brox. U-net: Convolutional networks for biomedical image segmentation. In Nassir Navab, Joachim Hornegger, William M. Wells, and Alejandro F. Frangi (eds.), *Medical Image Computing and Computer-Assisted Intervention – MICCAI 2015*, pp. 234–241, Cham, 2015. Springer International Publishing. ISBN 978-3-319-24574-4.

J. Rossignac. Edgebreaker: connectivity compression for triangle meshes. *IEEE Transactions on Visualization and Computer Graphics*, 5(1):47–61, 1999. doi: 10.1109/2945.764870.

William J. Schroeder, Jonathan A. Zarge, and William E. Lorensen. Decimation of triangle meshes. *SIGGRAPH Comput. Graph.*, 26(2):65–70, July 1992. ISSN 0097-8930. doi: 10.1145/142920.134010. URL https://doi.org/10.1145/142920.134010.

Sebastian Schwarz, Marius Preda, Vittorio Baroncini, Madhukar Budagavi, Pablo Cesar, Philip A Chou, Robert A Cohen, Maja Krivokuća, Sébastien Lasserre, Zhu Li, et al. Emerging mpeg standards for point cloud compression. *IEEE Journal on Emerging and Selected Topics in Circuits and Systems*, 9(1):133–148, 2018.

Yiting Shao, Xiaodong Yang, Wei Gao, Shan Liu, and Ge Li. 3d point cloud attribute compression using diffusion-based texture-aware intra prediction. *IEEE Transactions on Circuits and Systems for Video Technology*, 34(10):9633–9646, 2024. doi: 10.1109/TCSVT.2024.3396694.

Nicholas Sharp et al. Polyscope, 2019. www.polyscope.run.

William Shen and Willie McClinton. Accelerating nerfs: Optimizing neural radiance fields with specialized hardware architectures. Technical report, 2023. URL https://williamshen-nz.github.io/accelerating-nerfs/.

Jinglei Shi and Christine Guillemot. Distilled low rank neural radiance field with quantization for light field compression. *arXiv preprint arXiv:2208.00164*, 2022.

Seungjoo Shin and Jaesik Park. Binary radiance fields. *Advances in neural information processing systems*, 36, 2024.

Yawar Siddiqui, Antonio Alliegro, Alexey Artemov, Tatiana Tommasi, Daniele Sirigatti, Vladislav Rosov, Angela Dai, and Matthias Nießner. Meshgpt: Generating triangle meshes with decoder-only transformers. In *Proceedings of the IEEE/CVF Conference on Computer Vision and Pattern Recognition (CVPR)*, pp. 19615–19625, June 2024.

Vincent Sitzmann, Michael Zollhöfer, and Gordon Wetzstein. Scene representation networks: Continuous 3d-structure-aware neural scene representations. *Advances in Neural Information Processing Systems*, 32, 2019.

Vincent Sitzmann, Julien Martel, Alexander Bergman, David Lindell, and Gordon Wetzstein. Implicit neural representations with periodic activation functions. In H. Larochelle, M. Ranzato, R. Hadsell, M.F. Balcan, and H. Lin (eds.), *Advances in Neural Information Processing Systems*, volume 33, pp. 7462–7473. Curran Associates, Inc., 2020. URL https://proceedings.neurips.cc/paper_files/paper/2020/file/53c04118df112c13a8c34b38343b9c10-Paper.pdf.

Nitish Srivastava, Geoffrey Hinton, Alex Krizhevsky, Ilya Sutskever, and Ruslan Salakhutdinov. Dropout: A simple way to prevent neural networks from overfitting. *Journal of Machine Learning Research*, 15(56): 1929–1958, 2014. URL http://jmlr.org/papers/v15/srivastava14a.html.

Vitaly Surazhsky and Craig Gotsman. Explicit surface remeshing. In *Proceedings of the 2003 Eurographics/ACM SIGGRAPH symposium on Geometry processing*, pp. 20–30, 2003.

Andrzej Szymczak, Jarek Rossignac, and Davis King. Piecewise regular meshes: Construction and compression. *Graphical Models*, 64(3-4):183–198, 2002.

Towaki Takikawa, Joey Litalien, Kangxue Yin, Karsten Kreis, Charles Loop, Derek Nowrouzezahrai, Alec Jacobson, Morgan McGuire, and Sanja Fidler. Neural geometric level of detail: Real-time rendering with implicit 3D shapes. 2021.

Towaki Takikawa, Alex Evans, Jonathan Tremblay, Thomas Müller, Morgan McGuire, Alec Jacobson, and Sanja Fidler. Variable bitrate neural fields. In *ACM SIGGRAPH 2022 Conference Proceedings*, SIGGRAPH '22, New York, NY, USA, 2022. Association for Computing Machinery. ISBN 9781450393379. doi: 10.1145/3528233.3530727. URL https://doi.org/10.1145/3528233.3530727.

Matthew Tancik, Pratul Srinivasan, Ben Mildenhall, Sara Fridovich-Keil, Nithin Raghavan, Utkarsh Singhal, Ravi Ramamoorthi, Jonathan Barron, and Ren Ng. Fourier features let networks learn high frequency functions in low dimensional domains. In H. Larochelle, M. Ranzato, R. Hadsell, M.F. Balcan, and H. Lin (eds.), *Advances in Neural Information Processing Systems*, volume 33, pp. 7537–7547. Curran Associates, Inc., 2020. URL https://proceedings.neurips.cc/paper_files/paper/2020/file/55053683268957697aa39fba6f231c68-Paper.pdf.

Jiaxiang Tang, Xiaokang Chen, Jingbo Wang, and Gang Zeng. Compressible-composable nerf via rank-residual decomposition. In S. Koyejo, S. Mohamed, A. Agarwal, D. Belgrave, K. Cho, and A. Oh (eds.), *Advances in Neural Information Processing Systems*, volume 35, pp. 14798–14809. Curran Associates, Inc., 2022. URL https://proceedings.neurips.cc/paper_files/paper/2022/file/5ed5c3c846f684a54975ad7a2525199f-Paper-Conference.pdf.

Jiaxiang Tang, Hang Zhou, Xiaokang Chen, Tianshu Hu, Errui Ding, Jingdong Wang, and Gang Zeng. Delicate textured mesh recovery from nerf via adaptive surface refinement. In *Proceedings of the IEEE/CVF International Conference on Computer Vision (ICCV)*, pp. 17739–17749, October 2023.

Gabriel Taubin and Jarek Rossignac. Geometric compression through topological surgery. *ACM Trans. Graph.*, 17(2):84–115, April 1998. ISSN 0730-0301. doi: 10.1145/274363.274365. URL https://doi.org/10.1145/274363.274365.

Costa Touma and Craig Gotsman. Triangle mesh compression. *Proceedings - Graphics Interface*, pp. 26–34, 1998. ISSN 0713-5424. Graphics Interface '98 ; Conference date: 18-06-1998 Through 20-06-1998.

Aaron van den Oord, Oriol Vinyals, and koray kavukcuoglu. Neural discrete representation learning. In I. Guyon, U. Von Luxburg, S. Bengio, H. Wallach, R. Fergus, S. Vishwanathan, and R. Garnett (eds.), *Advances in Neural Information Processing Systems*, volume 30. Curran Associates, Inc., 2017. URL https://proceedings.neurips.cc/paper_files/paper/2017/file/7a98af17e63a0ac09ce2e96d03992fbc-Paper.pdf.

Jianqiang Wang, Dandan Ding, Zhu Li, Xiaoxing Feng, Chuntong Cao, and Zhan Ma. Sparse tensor-based multiscale representation for point cloud geometry compression. *IEEE Transactions on Pattern Analysis and Machine Intelligence*, 45(7):9055–9071, 2023. doi: 10.1109/TPAMI.2022.3225816.

Jiaxin Wang, Weichen Dai, Kangcheng Ma, and Wanzeng Kong. Neural radiance fields with hash-low-rank decomposition. *Applied Sciences*, 14(23), 2024. ISSN 2076-3417. doi: 10.3390/app142311277. URL https://www.mdpi.com/2076-3417/14/23/11277.

Christopher Wewer, Kevin Raj, Eddy Ilg, Bernt Schiele, and Jan Eric Lenssen. latentsplat: Autoencoding variational gaussians for fast generalizable 3d reconstruction. In *European Conference on Computer Vision*, pp. 456–473. Springer, 2024.

Shuang Wu, Youtian Lin, Yifei Zeng, Feihu Zhang, Jingxi Xu, Philip Torr, Xun Cao, and Yao Yao. Direct3d: Scalable image-to-3d generation via 3d latent diffusion transformer. In *The Thirty-eighth Annual Conference on Neural Information Processing Systems*, 2024. URL https://openreview.net/forum?id=vCOgjBIZuL.

Jianfeng Xiang, Xiaoxue Chen, Sicheng Xu, Ruicheng Wang, Zelong Lv, Yu Deng, Hongyuan Zhu, Yue Dong, Hao Zhao, Nicholas Jing Yuan, and Jiaolong Yang. Native and compact structured latents for 3d generation. *Tech report*, 2025a.

Jianfeng Xiang, Zelong Lv, Sicheng Xu, Yu Deng, Ruicheng Wang, Bowen Zhang, Dong Chen, Xin Tong, and Jiaolong Yang. Structured 3d latents for scalable and versatile 3d generation. In *Proceedings of the IEEE/CVF Conference on Computer Vision and Pattern Recognition (CVPR)*, pp. 21469–21480, June 2025b.

Xiufeng Xie, Riccardo Gherardi, Zhihong Pan, and Stephen Huang. Hollownerf: Pruning hashgrid-based nerfs with trainable collision mitigation. In *Proceedings of the IEEE/CVF International Conference on Computer Vision*, pp. 3480–3490, 2023.

Yiheng Xie, Towaki Takikawa, Shunsuke Saito, Or Litany, Shiqin Yan, Numair Khan, Federico Tombari, James Tompkin, Vincent sitzmann, and Srinath Sridhar. Neural fields in visual computing and beyond. *Computer Graphics Forum*, 41(2):641–676, 2022. doi: https://doi.org/10.1111/cgf.14505. URL https://onlinelibrary.wiley.com/doi/abs/10.1111/cgf.14505.

Jiale Xu, Weihao Cheng, Yiming Gao, Xintao Wang, Shenghua Gao, and Ying Shan. Instantmesh: Efficient 3d mesh generation from a single image with sparse-view large reconstruction models. *arXiv preprint arXiv:2404.07191*, 2024.

Xiaoxuan Yang, Guo Lu, Donghui Feng, Zhengxue Cheng, Guosheng Yu, and Li Song. Coarse-to-fine transformer for lossless 3d medical image compression. In *2024 IEEE International Conference on Visual Communications and Image Processing (VCIP)*, pp. 1–5, 2024. doi: 10.1109/VCIP63160.2024.10849903.

Yiying Yang, Wen Liu, Fukun Yin, Xin Chen, Gang Yu, Jiayuan Fan, and Tao Chen. Vq-nerf: Vector quantization enhances implicit neural representations. *arXiv preprint arXiv:2310.14487*, 2023.

Sergey Zakharov, Rares Andrei Ambrus, Katherine Liu, and Adrien Gaidon. Road: Learning an implicit recursive octree auto-decoder to efficiently encode 3d shapes. In Karen Liu, Dana Kulic, and Jeff Ichnowski (eds.), *Proceedings of The 6th Conference on Robot Learning*, volume 205 of *Proceedings of Machine Learning Research*, pp. 2136–2147. PMLR, 14–18 Dec 2023. URL https://proceedings.mlr.press/v205/zakharov23a.html.

Maciej Zamorski, Maciej Zięba, Piotr Klukowski, Rafał Nowak, Karol Kurach, Wojciech Stokowiec, and Tomasz Trzciński. Adversarial autoencoders for compact representations of 3d point clouds. *Computer Vision and Image Understanding*, 193:102921, 2020.

Xiaohui Zeng, Arash Vahdat, Francis Williams, Zan Gojcic, Or Litany, Sanja Fidler, and Karsten Kreis. Lion: Latent point diffusion models for 3d shape generation. In *Advances in Neural Information Processing Systems (NeurIPS)*, 2022.

Biao Zhang, Jiapeng Tang, Matthias Niessner, and Peter Wonka. 3dshape2vecset: A 3d shape representation for neural fields and generative diffusion models. *ACM Transactions On Graphics (TOG)*, 42(4):1–16, 2023.

Bowen Zhang, Tianyu Yang, Yu Li, Lei Zhang, and Xi Zhao. Compress3d: A compressed latent space for 3d generation from a single image. In Aleš Leonardis, Elisa Ricci, Stefan Roth, Olga Russakovsky, Torsten Sattler, and Gül Varol (eds.), *Computer Vision – ECCV 2024*, pp. 276–292, Cham, 2025a. Springer Nature Switzerland. ISBN 978-3-031-72649-1.

Jinzhi Zhang, Feng Xiong, and Mu Xu. 3d representation in 512-byte:variational tokenizer is the key for autoregressive 3d generation, 2024a. URL https://arxiv.org/abs/2412.02202.

Jinzhi Zhang, Feng Xiong, Guangyu Wang, and Mu Xu. G3pt: Unleash the power of autoregressive modeling in 3d generation via cross-scale querying transformer. In James Kwok (ed.), *Proceedings of the Thirty-Fourth International Joint Conference on Artificial Intelligence, IJCAI-25*, pp. 2350–2358. International Joint Conferences on Artificial Intelligence Organization, 8 2025b. doi: 10.24963/ijcai.2025/262. URL https://doi.org/10.24963/ijcai.2025/262. Main Track.

Junteng Zhang, Gexin Liu, Dandan Ding, and Zhan Ma. Transformer and upsampling-based point cloud compression. In *Proceedings of the 1st International Workshop on Advances in Point Cloud Compression, Processing and Analysis*, APCCPA '22, pp. 33–39, New York, NY, USA, 2022. Association for Computing Machinery. ISBN 9781450394918. doi: 10.1145/3552457.3555731. URL https://doi.org/10.1145/3552457.3555731.

Richard Zhang, Phillip Isola, Alexei A. Efros, Eli Shechtman, and Oliver Wang. The unreasonable effectiveness of deep features as a perceptual metric. In *2018 IEEE/CVF Conference on Computer Vision and Pattern Recognition*, pp. 586–595, 2018. doi: 10.1109/CVPR.2018.00068.

Zhiyu Zhang, Guo Lu, Huanxiong Liang, Zhengxue Cheng, Anni Tang, and Li Song. Rate-aware compression for nerf-based volumetric video. In *Proceedings of the 32nd ACM International Conference on Multimedia*, pp. 3974–3983, 2024b.

Zibo Zhao, Wen Liu, Xin Chen, Xianfang Zeng, Rui Wang, Pei Cheng, Bin Fu, Tao Chen, Gang Yu, and Shenghua Gao. Michelangelo: Conditional 3d shape generation based on shape-image-text aligned latent representation. *Advances in neural information processing systems*, 36:73969–73982, 2023.

Hongliang Zhong, Jingbo Zhang, and Jing Liao. Vq-nerf: Neural reflectance decomposition and editing with vector quantization. *IEEE Transactions on Visualization and Computer Graphics*, 30(9):6247–6260, 2023.

Yi Zhou, Chenglei Wu, Zimo Li, Chen Cao, Yuting Ye, Jason Saragih, Hao Li, and Yaser Sheikh. Fully convolutional mesh autoencoder using efficient spatially varying kernels. In H. Larochelle, M. Ranzato, R. Hadsell, M.F. Balcan, and H. Lin (eds.), *Advances in Neural Information Processing Systems*, volume 33, pp. 9251–9262. Curran Associates, Inc., 2020. URL https://proceedings.neurips.cc/paper_files/paper/2020/file/68dd09b9ff11f0df5624a690fe0f6729-Paper.pdf.

Denis Zorin, Peter Schröder, and Wim Sweldens. Interpolating subdivision for meshes with arbitrary topology. In *Proceedings of the 23rd annual conference on Computer graphics and interactive techniques*, pp. 189–192, 1996.

Appendix Contents

A Additional Implementation Details **25**

A.1 Network Design 25

A.2 Training 26

B Evaluation Details **27**

B.1 Metrics 27

B.2 Baselines 28

B.3 Collection of Additional Meshes for Evaluation 29

B.4 Collection of Additional Radiance Fields for Evaluation 30

C Additional Results **30**

C.1 Additional Results for Mesh Compression 30

C.2 Additional Results for Point Cloud Compression 30

C.3 Additional Results for Radiance Field Compression 30

C.4 Qualitative Results on Meshes 30

C.5 Ablations 31

C.6 Failure Cases 31

C.7 Robustness to Input Noise 34

C.8 Decoder Amortization 34

D Additional Related Works **35**

E Results Library **36**

A Additional Implementation Details

We share additional implementation details to reproduce SQUEEZE3D.

A.1 Network Design

For each of the encoder-decoder pairs, we train the mapping networks, which are feed-forward neural networks. We summarize network architectures in Figure 8. Our architectures for different representations are highly similar.

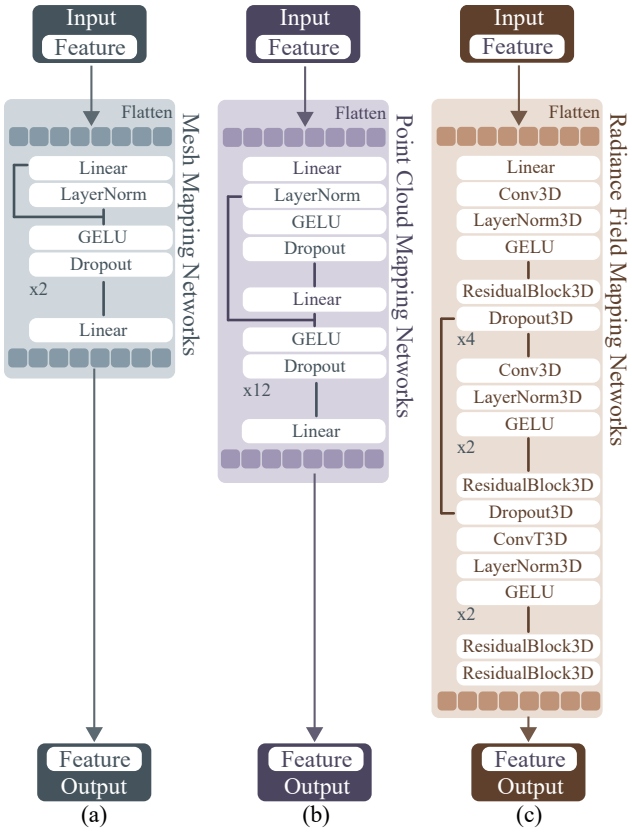


Figure 8: **Network Architectures.**

Meshes. The mapping networks together first flatten the input and apply a linear layer to project it into a hidden dimension. This is followed by LayerNorm (Ba et al., 2016), a GELU nonlinearity (Hendrycks & Gimpel, 2023), and dropout (Srivastava et al., 2014). A second linear layer then produces another hidden representation, which is added residually to the output of the first linear layer and passed through a second LayerNorm. After another GELU and dropout, a final linear transformation projects into the latent space.

Point Clouds. The mapping networks together consist of flattening the input and feeding it through a linear projection and LayerNorm (Ba et al., 2016); this normalised vector is stored as a global residual. The sequence then passes through GELU-activated (Hendrycks & Gimpel, 2023) hidden layers of uniform width, each followed by dropout regularisation on the activations (Srivastava et al., 2014). We use two skip-connection schemes: (i) the global residual is re-added immediately after the first hidden layer, and (ii) every fourth hidden layer receives a local residual that adds its own input to its output, creating short four-layer paths. A final linear projection transforms the resulting representation into the target latent space.

Radiance Fields. The mapping networks together consist of a custom LayerNorm that first permutes tensors so that LayerNorm (Ba et al., 2016) can operate across channels before restoring the usual NCDHW layout. We then build ResidualBlocks, which mirror a bottleneck ResNet-V2 design (He et al., 2016): a $3 \times 3 \times 3$ conv–LN–GELU (Hendrycks & Gimpel, 2023) stem, a $1 \times 1 \times 1 \to 3 \times 3 \times 3$ bottleneck branch that doubles the channel count, and two skip paths: (i) projection shortcut for stride/width mismatches and (ii) "within-block" residual that re-adds the pre-bottleneck activation just before the final GELU. The encoder begins with a 96-channel input, expands to 192 channels, and applies two strided ResidualBlock units to down-sample from 40^3 latents to 20^3 and then 10^3. Thus we have a narrow bottleneck of 24 channels that serves as the latent code. The symmetric decoder inverts this pathway with a $3 \times 3 \times 3$ convolution, residual processing, and two transposed-conv up-sampling stages that restore the original resolution, all regularised by spatial Dropout in 3D. U-Net–style (Ronneberger et al., 2015) skip connections add encoder feature maps to decoder activations whenever spatial dimensions match.

In all cases the reverse mapping network produces a single flat vector whose dimensionality equals the flattened size of the target decoder's latent, and a fixed reshape maps it to the structure the decoder expects. Thus, we use no decoder-specific architectures. For InstantMesh and LRM, the decoder takes a triplane, so the final linear layer produces $3 \times 80 \times 64 \times 64$ values that are reshaped into the $(3, 80, 64, 64)$ triplane tensor before being passed to the frozen triplane decoder. For LION, whose latent is an unordered set rather than a

grid, the latent is a fixed-size concatenation of a global shape code and a per-point local code; the network outputs an 8320-dimensional vector that we split into the first 128 dimensions (the global latent, reshaped to $1 \times 128 \times 1 \times 1$) and the remaining 8192 dimensions (the local latent, reshaped to $1 \times 8192 \times 1 \times 1$). Because the local code has a fixed length and canonical ordering, the mapping network never has to predict a variable-size or permutation-invariant point set directly.

A.2 Training

Our results are collected on a machine with either 1×NVIDIA RTX 4090 GPU or $1-4\times$ H100 GPUs. We list the choices we make during training for each encoder-generator pair.

For all the models we train with MeshAnything (Chen et al., 2025c) as the encoder, we use the 350-million-parameter version of MeshAnything and use the features created by MeshAnything as the encoded inputs. These encoded inputs `(257, 1024)` are relatively larger compared to our desired compression size.

MeshAnything (Chen et al., 2025c)-InstantMesh (Xu et al., 2024). While generating the dataset, we ensure that the input condition images are in the RGBA format and have no background. We experiment with having the mapping networks generate multiview ViT embeddings (Dosovitskiy et al., 2021) that InstantMesh uses, as well as the triplane representation InstantMesh uses. We observed better performance when generating triplane representations; thus, we report results for this setting.

MeshAnything (Chen et al., 2025c)-Open LRM (Hong et al., 2024; He & Wang, 2023). While generating the dataset, we ensure that the input condition images are in the RGBA format and have no background. Due to the lack of public code for the LRM, we use the OpenLRM implementation. We experiment with both `openlrm-mix-base-1.1` and `openlrm-obj-base-1.1`, and we observe that `openlrm-obj-base-1.1` performs better. We train the mapping networks to generate the triplane latents for LRM.

MeshAnything (Chen et al., 2025c)-Shap-E (Jun & Nichol, 2023). We experiment with Shap-E in the text-to-3D mode. The mapping networks generate the implicit MLP representations.

PointNet++ (Qi et al., 2017)-LION (Zeng et al., 2022). We experiment with the `SSG` and `MSG` versions of PointNet++ and observe that `SSG` without normals works best. We use the PointNet++ checkpoints pre-trained for classification. We consider the outputs from the point set feature learning module as the encoded representations. We use the `all` categories model for LION. The mapping networks are trained to generate both the global and local latents for LION. The same synthetic LION paired-latent dataset is shared across all compressed-dimensionality variants in Table 11.

We provide the model sizes in Table 9, compressed latent sizes in Table 11, one-time measured costs in Table 12, hyperparameters in Table 13, and latent-space sizes in Table 10.

Table 9: **Model Sizes.** Combined parameter count of the forward and reverse mapping networks trained for each setting.

Encoder-Decoder Pair	Parameters (M)
MeshAnything (Chen et al., 2025c)-InstantMesh (Xu et al., 2024)	96.12
MeshAnything (Chen et al., 2025c)-Open LRM (Hong et al., 2024; He & Wang, 2023)	87.51
MeshAnything (Chen et al., 2025c)-Shap-E (Jun & Nichol, 2023)	134.53
PointNet++ (Qi et al., 2017)-LION (Zeng et al., 2022) (512/1024)	2.11
PointNet++ (Qi et al., 2017)-LION (Zeng et al., 2022) (2048)	6.53
PointNet++ (Qi et al., 2017)-LION (Zeng et al., 2022) (4096)	22.29
PointNet++ (Qi et al., 2017)-LION (Zeng et al., 2022) (8192)	81.48
NeRF-MAE (Irshad et al., 2024)	86.46

Table 10: **Latent Space Sizes.** Sizes of latent spaces for encoder and generator models we use.

Encoder/Generator Model	Latent Space Size
MeshAnything (Chen et al., 2025c)	257×1024
InstantMesh TriPlane Features (Xu et al., 2024)	$3 \times 80 \times 64 \times 64$
LION (Zeng et al., 2022)	8320
PointNet++ (Qi et al., 2017)	1024
NeRF-MAE (Irshad et al., 2024)	$256 \times 20 \times 20 \times 20$

Table 11: **Latent Sizes.** The sizes of the compressed representations for our experiments.

Encoder → decoder	d_C	Latent size (KB)
MeshAnything → OpenLRM	1024	4.00
MeshAnything → Shap-E	1024	4.00
MeshAnything → InstantMesh	770	3.01
PointNet++ → LION	512	2.00
PointNet++ → LION	1024	4.00
PointNet++ → LION	2048	8.00
PointNet++ → LION	4096	16.00
PointNet++ → LION	8192	32.00
NeRF-MAE → NeRF-MAE	24000	93.75

Table 12: **One-time Training and Data-creation Costs.** These costs are incurred once for the listed encoder-generator setting; subsequent objects use feed-forward inference.

Decoder	Mapping training (h)	Paired-data creation (h)
InstantMesh	12	20
LION	5	20
NeRF-MAE	15	3

B Evaluation Details

SQUEEZE3D leverages pre-trained generative priors strictly as a decoding mechanism for compressing arbitrary 3D data, distinct from compressing the native outputs of generative models. Direct native encoder-decoder comparisons are possible for Shap-E, LION, and NeRF-MAE, as reported in Section 4.6. They are not available for feed-forward image-to-3D models such as InstantMesh and LRM, which lack native 3D encoders and would require a lossy intermediate rendering step.

B.1 Metrics

For all mesh and radiance-field experiments, the image-quality metrics (PSNR, MS-SSIM, LPIPS) are computed on rendered views: we render both the reference and the decompressed asset from 36 viewpoints placed on a sphere using a Fibonacci lattice, at a resolution of 512×512 with a perspective camera and Phong shading, and average each metric over all views and all objects. The geometric distortion metrics (Chamfer Distance, EMD) are computed on 2048 points sampled from each surface, with both point sets normalized into the unit cube $[0, 1]^3$.

In addition to file-relative compression ratios, we report standardized rates in Table 14. Mesh rates are bits per input vertex and point-cloud rates are bits per input point; lower values indicate smaller compressed representations for a fixed input element count.

Table 13: **Training Hyperparameters.** We show the training hyperparameters for the mapping networks we train.

Hyperparameter	LRM	Shap-E	InstantMesh	NeRF-MAE
Training Precision	FP-32	FP-32	FP-32	FP-32
d_C	1024	1024	770	24000
Dropout	0.35	0.35	0.35	0.2
Epochs	700	700	700	200
Batch Size	16	8	16	4
Optimizer	Muon	Adam	Muon	Muon
Optimizer Parameters	NS = 6 $\beta = 0.95$	$\lambda = 10^{-2}$ $\beta_1 = 0.9$ $\beta_2 = 0.999$	NS = 6 $\beta = 0.95$	NS = 6 $\beta = 0.95$
Initial Learning Rate	10^{-2}	10^{-4}	10^{-3}	10^{-2}
Final Learning Rate	10^{-7}	10^{-4}	10^{-7}	10^{-5}
Scheduler	Linear Decay	Constant	Linear Decay	Linear Decay
Decay Epochs	700	N/A	600	100
Gradient Accum. Steps	1	2	1	1
Gradient Clipping	None	None	None	None

Hyperparameter	LION (512/1024)	LION (2048)	LION (4096)	LION (8192)
Training Precision	FP-32	FP-32	FP-32	FP-32
d_C	512/1024	2048	4096	8192
Dropout	0.3	0.3	0.3	0.3
Epochs	400	400	400	400
Batch Size	16	16	16	16
Optimizer	Muon	Muon	Muon	Muon
Optimizer Parameters	$\beta = 0.95$ NS = 6	$\beta = 0.95$ NS = 6	$\beta = 0.95$ NS = 6	$\beta = 0.95$ NS = 6
Initial Learning Rate	10^{-3}	10^{-3}	10^{-3}	10^{-3}
Final Learning Rate	10^{-7}	10^{-7}	10^{-7}	10^{-7}
Scheduler	Linear Decay	Linear Decay	Linear Decay	Linear Decay
Decay Epochs	100	100	100	100
Gradient Accum. Steps	1	1	1	1
Gradient Clipping	None	None	None	None

B.2 Baselines

We compare Squeeze3D against established compression methods for each representation, described below. For radiance fields we compare against codecs applicable to arbitrary (rgbσ) grids, as most NeRF and 3D Gaussian Splat (3DGS)-specific methods do not apply to our setting.

Draco. Draco (Galligan et al., 2018) is a non-learned codec that we apply to both meshes and point clouds. We always use a compression level of 10 and report several quantization settings, given as the number of bits for the position / texture-coordinate / normal / generic attributes: § uses 14/14/14/14, ‡ uses 11/10/8/8, † uses 7/7/7/7, and * uses 4/4/4/4. For meshes we report all four settings; for point clouds we report the ‡ and § settings.

Corto. We compress meshes with Corto (Lab, 2025) using 4-bit quantization for both the normal and texture-coordinate attributes, with the texture image stored separately. The compressed size is read directly from the encoder output.

Table 14: **Standardized Rate Measures.** Bits per input vertex for mesh compression and bits per input point for point-cloud compression.

Mesh method	Bits/vertex ↓	Point-cloud method	Bits/point ↓
Draco* (Galligan et al., 2018)	141.06	Draco‡ (Galligan et al., 2018)	29.92
Draco† (Galligan et al., 2018)	145.61	Draco§ (Galligan et al., 2018)	20.88
Draco‡ (Galligan et al., 2018)	147.13	G-PCC (Schwarz et al., 2018)	12.60
Draco§ (Galligan et al., 2018)	157.75	V-PCC (Liu et al., 2019)	<u>9.32</u>
Corto (Lab, 2025)	21.24	SparsePCGC (Wang et al., 2023)	13.89
Neural Subd. (Liu et al., 2020a)	86.46	SQUEEZE3D (LION, $d_C = 512$)	**8.00**
DeepSDF (Park et al., 2019)	7.58		
NGF (Edavamadathil Sivaram et al., 2024)	22.75		
3DShape2VecSet (Zhang et al., 2023)	<u>2.86</u>		
SQUEEZE3D (InstantMesh)	**0.46**		

Neural Subdivision. Neural Subdivision (Liu et al., 2020a) learns to refine a coarse mesh. We train the per-object network for 700 epochs (learning rate 2×10^{-3}) and apply 2 subdivision levels at inference; its three sub-networks (initialization, edge, and vertex) each use two hidden layers of width 32.

DeepSDF. DeepSDF (Park et al., 2019) represents a shape as a latent code decoded by an 8-layer, width-512 MLP (the code is injected at the middle layer, with dropout 0.2), trained with code regularization for 2001 epochs. The compressed representation is the per-shape 256-dimensional FP-32 latent code (1 KB).

Neural Geometry Fields (NGF). NGF (Edavamadathil Sivaram et al., 2024) fits a neural displacement field over a coarse base mesh. We use 1000 patches with 20-dimensional feature vectors and optimize each object over base resolutions $\{4, 8, 12, 16\}$ for 100 iterations each (Adam, learning rate 10^{-3}); the compressed size is the serialized feature stream.

3DShape2VecSet. We use the pre-trained shape autoencoder of 3DShape2VecSet (Zhang et al., 2023) (the `kl_d512_m512_l8` variant) as a learned mesh-compression baseline. To compress a mesh, we sample 2048 points on its surface and encode them into a set of 512 latent vectors of dimension 8; this 512×8 latent is the compressed geometry. To decompress, we evaluate the decoder's occupancy field on a 128^3 grid and extract the surface using Marching Cubes.

G-PCC. G-PCC (Schwarz et al., 2018) is the MPEG geometry-based point-cloud coding standard, which we evaluate on point clouds using the TMC13 reference software.

V-PCC. V-PCC (Liu et al., 2019) is the MPEG video-based point-cloud coding standard, evaluated with the TMC2 reference software. We encode with a 3D coordinate bit depth of 10 and geometry QP 32, a single 8-bit colour attribute at QP 28, occupancy-map precision 4, and a maximum depth of 12.

SparsePCGC. SparsePCGC (Wang et al., 2023) is a multiscale sparse-convolution codec. For point clouds, we evaluate the released checkpoints and report the resulting operating point in Tables 3 and 14. For radiance-field (rgbσ) grids, we use its 8-stage model with kernel size 5 and obtain different rate points by varying the position quantization scale.

VQRF. VQRF (Li et al., 2023a) compresses radiance-field grids through voxel pruning and vector quantization. We use a codebook of 4096 entries together with importance-based voxel pruning (inclusion and pruning thresholds of 0.6 and 0.999).

B.3 Collection of Additional Meshes for Evaluation

Since SQUEEZE3D is designed as a compression-decompression framework that should not require per-scene retraining, the generalization capability of our mapping networks to unseen 3D models is very important. Thus, we also collected a very diverse dataset of 500 high-quality 3D meshes from the following sources:

- OpenLRM Demo: `https://huggingface.co/spaces/zxhezexin/OpenLRM`

- InstantMesh Demo: `https://huggingface.co/spaces/TencentARC/InstantMesh`
- Hunyuan3D-2 Demo: `https://huggingface.co/spaces/tencent/Hunyuan3D-2`
- TRELLIS Demo: `https://huggingface.co/spaces/JeffreyXiang/TRELLIS`
- SPAR3D Demo: `https://huggingface.co/spaces/stabilityai/stable-point-aware-3d`
- SORA-3D Demo: `https://huggingface.co/spaces/ginipick/SORA-3D`
- A subset of ABO (Collins et al., 2022) composed of 384 meshes

B.4 Collection of Additional Radiance Fields for Evaluation

Since SQUEEZE3D is designed as a compression-decompression framework that should not require per-scene retraining, the generalization capability of our mapping networks to unseen 3D models is very important. Thus, we also report results on the unseen "ai" subset of the NeRF-MAE dataset (Irshad et al., 2024).

C Additional Results

C.1 Additional Results for Mesh Compression

We show the results for mesh compression on our test set, or the $\mathcal{T}$ set, with 3D metrics (Chamfer distance and EMD) as well as wall-clock times for compression and decompression in Table 15.

C.2 Additional Results for Point Cloud Compression

We report point-cloud geometry metrics in Table 17 and rate-distortion behavior in Figure 10.

C.3 Additional Results for Radiance Field Compression

Our mapping networks are trained on the dataset we derived from NeRF-MAE (Irshad et al., 2024), but we test SQUEEZE3D on only the radiance fields in the `ai` subset of the dataset, which was collected separately from the other datasets. On our collection of radiance fields, SQUEEZE3D achieves on average only a 4.22 dB reduction in the PSNR as we show in Table 16.

C.4 Qualitative Results on Meshes

We also notice that our approach works well with high-resolution complex meshes as we show in Figure 14. In Figure 11, we show a mesh we reconstruct with our method from multiple camera angles to demonstrate that our approach learns a correct transformation between the latent spaces and the reconstruction is consistent. We also observe that the compressed representation our method learns can be interpolated as we show in Figure 9. In Figure 13 we show examples using two different generative models indicating that SQUEEZE3D can be extended to use other generative models for compression. In Figure 12, we observe that our method learns to effectively represent intricate geometrical details.

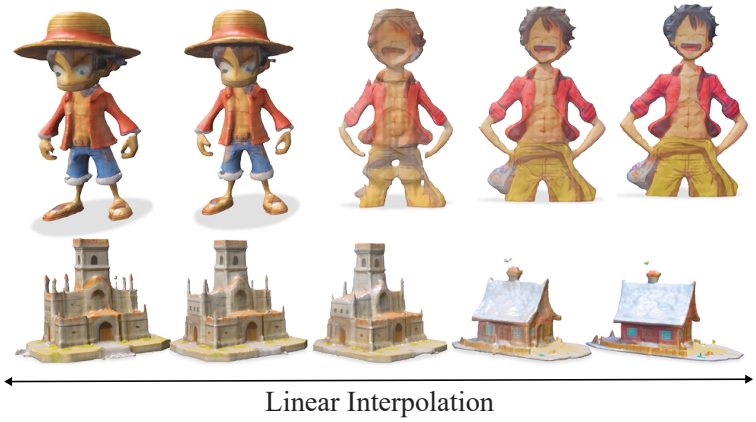


Figure 9: **Interpolation.** The compressed representations we obtain can also be interpolated. In these examples, we obtain the compressed representation for the leftmost and rightmost meshes and linearly interpolate between them.

Table 15: **Mesh Compression.** Quantitative comparison of SQUEEZE3D with state-of-the-art 3D mesh compression methods, including geometry-based metrics Chamfer Distance and EMD. We also report the compression and decompression wall-clock times. All quality metrics are reported on our Objaverse test set, denoted $\mathcal{T}$.

Method	CR (×) (MB) ↑	Compress (ms) ↓	Decompress (ms) ↓	$\mathcal{T}$-PSNR ↑	$\mathcal{T}$-MS-SSIM ↑	$\mathcal{T}$-LPIPS ↓	$\mathcal{T}$-Chamfer ↓	$\mathcal{T}$-EMD ↓
Draco* (Galligan et al., 2018)	6.92 (6.43 / 0.93)	70.30	29.97	15.45 (±1.27)	0.7468 (±0.09)	0.2437 (±0.09)	1.2746	0.0544
Draco† (Galligan et al., 2018)	6.70 (6.43 / 0.96)	69.05	28.33	23.33 (±1.32)	0.9576 (±0.03)	0.1039 (±0.06)	0.8739	0.0385
Draco‡ (Galligan et al., 2018)	6.61 (6.43 / 0.97)	68.15	27.46	38.91 (±1.30)	0.9992 (±0.00)	0.0045 (±0.00)	0.4214	0.0108
Draco§ (Galligan et al., 2018)	6.20 (6.43 / 1.04)	66.30	25.81	**48.55** (±1.54)	**1.0000** (±0.00)	**0.0004** (±0.00)	**0.2060**	**0.0044**
Corto (Lab, 2025)	45.93 (6.43 / 0.14)	50.52	8.20	20.92 (±2.79)	0.8619 (±0.08)	0.1374 (±0.08)	0.9644	0.0438
Neural Subd. (Liu et al., 2020a)	11.28 (6.43 / 0.57)	61104.12	**0.00**	15.95 (±2.18)	0.8525 (±0.04)	0.1513 (±0.05)	1.1125	0.0496
DeepSDF (Park et al., 2019)	131.22 (6.43 / 0.05)	887.78	578.53	8.47 (±0.23)	0.7039 (±0.07)	0.3704 (±0.08)	1.5842	0.0617
NGF (Edavamadathil Sivaram et al., 2024)	42.87 (6.43 / 0.15)	152637.87	507.21	35.45 (±3.02)	0.9987 (±0.08)	0.0054 (±0.03)	0.3866	0.0130
3DShape2VecSet (Zhang et al., 2023)	342.50 (6.43 / 0.0188)	**4.90**	373.00	21.65 (±2.22)	0.9047 (±0.06)	0.1582 (±0.09)	0.5304	0.0101
SQUEEZE3D (InstantMesh)	**2187.07** (6.43 / 0.003)	270.24	1476.00	27.50 (±3.13)	0.9796 (±0.02)	0.0274 (±0.02)	0.3930	0.0084

Table 16: **Radiance Field Results.** Quantitative comparison of SQUEEZE3D for compressing radiance fields from the ai subset of the NeRF-MAE dataset (Section B.4).

Method	CR (×) (MB) ↑	Compress (ms) ↓	Decompress (ms) ↓	PSNR ↑	MS-SSIM ↑	LPIPS ↓
Ours	657.89 (59.21 / 0.09)	45.63	75.80	22.40	0.8958	0.1400

Table 17: **Point Cloud Compression with Geometry Metrics.** Quantitative comparison of SQUEEZE3D with state-of-the-art point cloud compression methods, including geometry-based metrics Chamfer Distance and EMD.

Method	CR (×) (KB) ↑	Compress (ms) ↓	Decompress (ms) ↓	PCQM ↑	PointSSIM ↑	Chamfer ↓	EMD ↓
Draco‡ (Galligan et al., 2018)	15.64 (117 / 7.48)	0.35	0.34	**3.2875** (± 0.13)	**0.9722** (± 0.11)	**0.0284**	**0.0061**
Draco§ (Galligan et al., 2018)	22.41 (117 / 5.22)	**0.25**	**0.23**	2.1039 (± 0.08)	0.9535 (± 0.12)	0.0419	0.0095
SQUEEZE3D (LION)	**58.50** (117 / 2.00)	3.85	12.74	1.8437 (± 1.13)	0.4484 (± 0.11)	0.0285	0.0062

C.5 Ablations

We conduct several ablation studies to better understand the behavior of SQUEEZE3D and analyze the trade-offs between compression ratio, reconstruction quality, and computational efficiency. First, we investigate how varying the size of our compressed representation affects decompression time. In Table 18 on a separate test set of 100 point clouds, we show that increasing the compressed size modestly increases compression and decompression times because it changes the size of the mapping networks. Next, we examine how different compression sizes affect reconstruction quality. Table 18 shows a correlation between latent dimension and reconstruction quality. We observe substantial improvements in PointSSIM when increasing the compressed size from 1024 to 2048; however, this improvement in quality starts diminishing beyond the compressed size of 2048. We perform an ablation of training with and without Gram loss (Section 3.2) in Table 19.

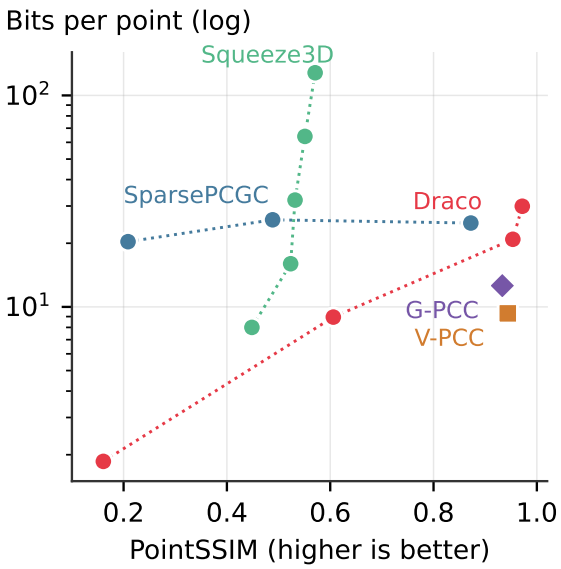


Figure 10: **Point-cloud rate–distortion.** PointSSIM (x-axis) versus bits/input point (log y-axis) for SQUEEZE3D and four codecs. Each SQUEEZE3D point uses separately trained mappings.

C.6 Failure Cases

To better understand the limitations of our approach, we analyze failure cases where SQUEEZE3D struggles to faithfully reconstruct the input geometry.



Figure 11: **Multi-view visualization of compressed and reconstructed meshes.** The consistent appearance across different viewing angles demonstrates that Squeeze3D learns correct transformations between latent spaces and produces coherent 3D reconstructions. This confirms that our compressed representation encodes complete 3D information rather than view-dependent features.

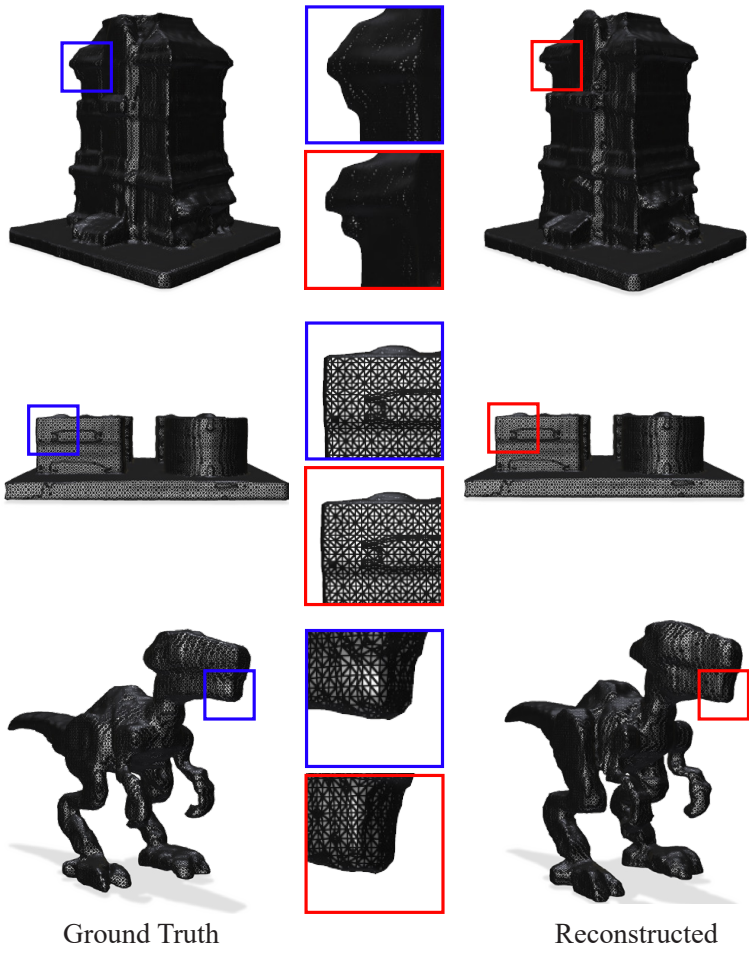


Figure 12: **Squeeze3D preserves geometry details.** We show some meshes compressed with Squeeze3D as wireframes. Notice that Squeeze3D preserves many fine-grained geometric details.

The primary cause of failure stems from the dependency on the generator's prior distribution. When the input geometry significantly deviates from the distribution of shapes the generator was trained on, the generator may fail to produce the correct details, or the mapping network may fail to find a corresponding code in the generator's latent space that represents the input. We illustrate these failure cases in Figure 15 and Table 20.

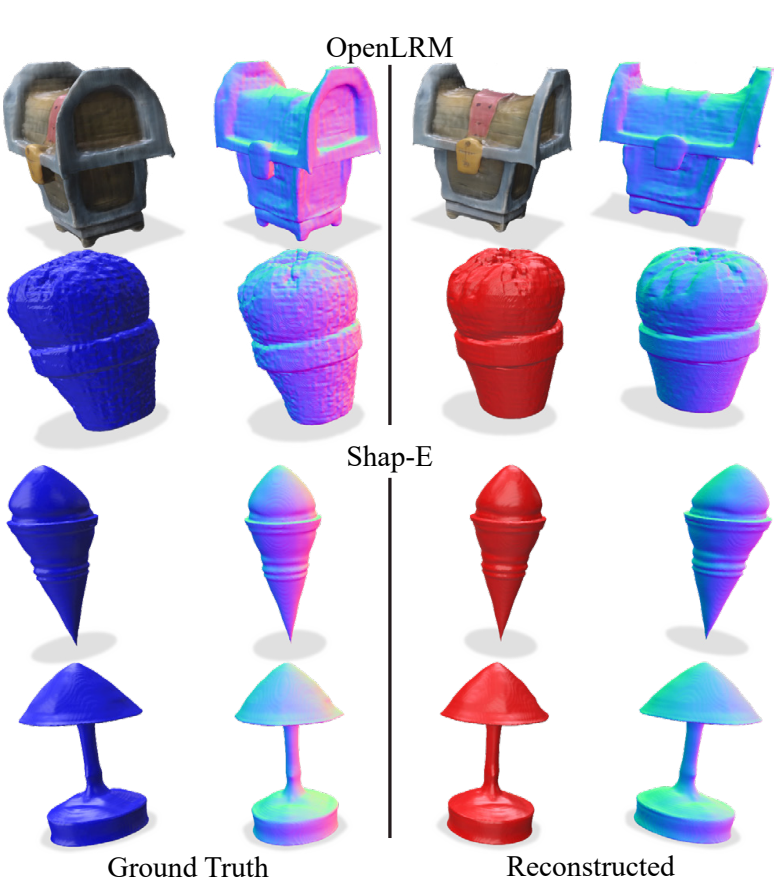


Figure 13: **Compression results using different 3D generators.** SQUEEZE3D is agnostic to the choice of a 3D generation model. Thus, we show compression results with the 3D generators OpenLRM and Shap-E. We choose 3D meshes that lie within the representational capacity of the chosen 3D generators.



Figure 14: **Compressing Complex Meshes.** SQUEEZE3D can be used to compress highly complex textured 3D meshes (in this case 77851 vertices and 120812 faces).

Table 18: **Ablations.** Ablation study on compressed representation size. We analyze how varying the dimensionality of the compressed latent space affects compression time, decompression time, and reconstruction quality (measured by PCQM and PointSSIM).

Size ($\mathbf{z}_{\text{comp}}$)	Compression (ms)	Decompression (ms)	PCQM ↑	PointSSIM ↑
512	**3.85**	**12.74**	1.4001	0.3640
1024	**3.85**	**12.74**	1.4047	0.3640
2048	<u>4.22</u>	<u>13.39</u>	1.3311	0.4249
4096	4.85	14.04	**1.8437**	<u>0.4318</u>
8192	5.30	14.19	<u>1.5665</u>	**0.4473**

We primarily observe loss of fine details, where highly intricate structures or text that are not well-represented in the generator's latent space are smoothed out or ignored. This limitation can be due to: (1) The encoder may fail to capture high-frequency details. (2) Even if the encoder captures these details, the generator's latent bottleneck may filter them out.

To identify which component limits these examples, we decode the MeshAnything representation using its native decoder and also reconstruct each object directly with InstantMesh, bypassing our mapping networks.

Table 19: **Ablation.** Quantitative comparison of SQUEEZE3D (InstantMesh) with and without Gram-loss.

Method	CR (×) (MB) ↑	Compress (ms) ↓	Decompress (ms) ↓	PSNR ↑	MS-SSIM ↑	LPIPS ↓
SQUEEZE3D (InstantMesh)	**2187.07** (6.43 / 0.003)	**270.24**	**1476.00**	**27.50** (±3.13)	**0.9796** (±0.02)	**0.0274** (±0.02)
w/o Gram-loss	**2187.07** (6.43 / 0.003)	**270.24**	**1476.00**	24.20 (±3.50)	0.9205 (±0.04)	0.1321 (±0.035)



Figure 15: **Failure Cases.** We show examples where SQUEEZE3D fails to accurately reconstruct the input. (Left) Input mesh with highly intricate details or text. (Right) The reconstruction is smoothed, losing the fine-grained text or surface texture.

Table 20: **Quantitative failure-case analysis.** Image metrics are means over 36 geometry-only views; normalized Chamfer distance and approximate 3D EMD use 2,048 surface samples. Both meshes are independently normalized to a unit box without rigid ICP alignment.

Case	PSNR (↑)	MS-SSIM (↑)	LPIPS (↓)	Chamfer (↓)	EMD (↓)
XYZRGB Dragon	21.13	0.9315	0.0611	0.05154	0.12827
Lucy	19.47	0.8979	0.1043	0.19425	0.35322

The MeshAnything result is selected from one greedy and three stochastic decodes; the InstantMesh result is selected from two fixed-seed reconstructions conditioned directly on the six target views without Zero123Plus. As shown in Table 21, the native MeshAnything reconstruction substantially improves both failures. Direct InstantMesh reconstruction remains worse than native MeshAnything for both objects. These results indicate that the generator prior is the dominant quality ceiling for these cases.

C.7 Robustness to Input Noise

We perform a sensitivity analysis by adding zero-mean i.i.d. Gaussian noise to the vertices of every mesh in the $\mathcal{T}$-set and rerunning the complete encoder–mapping–generator pipeline. Here σ is the per-axis standard deviation expressed as a fraction of each clean mesh's bounding-box diagonal. For each mesh, we use the same noise directions, sampled faces, and barycentric coordinates at every noise level. Table 22 indicates modest changes at the smallest perturbation and increasingly strong degradation at larger noise levels.

We analogously evaluate radiance-field sensitivity by adding zero-mean i.i.d. Gaussian noise to every (rgbσ) grid in the radiance-field $\mathcal{T}$-set. Here σ is expressed as a fraction of each input's dynamic range. Table 23 shows gradual degradation as the perturbation increases.

C.8 Decoder Amortization

We define decoder amortization as the number of objects after which storing the frozen decoder and reverse mapping network once plus the compressed latent for each object uses no more storage than the original objects. For shared decompression storage S_{shared}, average original size S_{orig}, and per-object latent size S_{latent}, the break-even count is $\lceil S_{\text{shared}}/(S_{\text{orig}} - S_{\text{latent}})\rceil$. Table 24 reports the thresholds.

Table 21: **Failure attribution.** For the encoder-side test, we decode the MeshAnything representation using one greedy and three stochastic native autoregressive decodes and select the lowest-Chamfer result. For the generator-side test, we condition frozen InstantMesh directly on six target views, bypass Zero123Plus, evaluate two fixed seeds, and select the lower-Chamfer result.

Case	Reconstruction path	PSNR (↑)	MS-SSIM (↑)	LPIPS (↓)	Chamfer (↓)	EMD (↓)
XYZRGB Dragon	Native MeshAnything	22.93	0.9600	0.0321	0.01670	0.01936
XYZRGB Dragon	Direct InstantMesh	18.21	0.8795	0.1093	0.15039	0.28745
Lucy	Native MeshAnything	24.19	0.9607	0.0422	0.02736	0.07611
Lucy	Direct InstantMesh	21.25	0.9252	0.0743	0.05875	0.07850

Table 22: **Input-noise sensitivity.**

σ / bbox diagonal	PSNR (↑)	MS-SSIM (↑)	LPIPS (↓)	Chamfer (↓)	EMD (↓)
0 (clean)	**27.50**	**0.9796**	**0.0274**	**0.3930**	**0.0084**
0.005	<u>26.49</u>	<u>0.9767</u>	<u>0.0329</u>	<u>0.4517</u>	<u>0.0174</u>
0.010	24.19	0.9663	0.0533	0.6257	0.0204
0.025	20.12	0.9280	0.1369	1.1186	0.0305
0.050	19.07	0.9125	0.1916	1.9091	0.0954
0.100	18.54	0.9046	0.2140	2.0378	0.1107

Table 23: **Radiance-field input-noise sensitivity.** Gaussian noise scale is expressed relative to the input dynamic range.

σ / input dynamic range	PSNR (↑)	MS-SSIM (↑)	LPIPS (↓)
0 (clean)	**26.62**	**0.9533**	**0.0743**
0.005	<u>26.55</u>	<u>0.9528</u>	<u>0.0752</u>
0.010	26.43	0.9520	0.0768
0.025	26.10	0.9498	0.0805
0.050	25.62	0.9460	0.0869
0.100	24.90	0.9395	0.0980

D Additional Related Works

While we are interested in learning-based methods for compression, we include classical compression techniques, which are only tangentially related to our work, for completeness. These include approaches that reorder the structure of triangles and faces in the mesh to enable compressed encodings of elements based on their local structure and perform quantization (Deering, 1995; Taubin & Rossignac, 1998; Rossignac, 1999; Touma & Gotsman, 1998; Galligan et al., 2018). Most of these techniques are lossless and thus achieve high fidelity; however, they are inherently limited in their ability to significantly reduce file sizes since they preserve all details of the mesh representation. To overcome the limitations of lossless compression, lossy techniques have emerged as popular alternatives. Geometry simplification methods aim to reduce the number of polygons in a mesh while retaining as much of the original structure as possible (Lescoat et al., 2020; Garland & Heckbert, 1997; Surazhsky & Gotsman, 2003; Szymczak et al., 2002). Extensions of these methods have incorporated surface intrinsic properties, such as the mesh Laplacian, as a basis for simplification (Lescoat et al., 2020) or error metrics (Garland & Heckbert, 1997; Cohen et al., 1998) and coupled this with entropy coding (Lab, 2025). Recently, there have also been approaches that couple these with learned models (Potamias et al., 2022).

Traditional subdivision algorithms (Zorin et al., 1996; Catmull & Clark, 1998; Loop, 1987) refine coarse meshes by splitting polygonal faces into finer elements, often paired with displacement mapping (Hoppe et al., 1994) to enhance detail. However, these methods rely on hard-coded priors and fixed polynomial

Table 24: **Decompression-side amortization thresholds.** Exact break-even calculations including both the frozen decoder and reverse mapping network.

Decoder	Shared storage	Original/object	Latent/object	Break-even objects
Shap-E	2.89 GB	6.43 MB	4.00 KB	449
InstantMesh	3.43 GB	6.43 MB	3.01 KB	534
OpenLRM	2.79 GB	6.43 MB	4.00 KB	435
LION ($d_C = 512$)	312.25 MB	117 KB	2.00 KB	2,716
NeRF-MAE	478.92 MB	58.07 MB	93.75 KB	9

interpolations, which can overly smooth the reconstructed geometry and fail to capture intricate details. Neural approaches (Hertz et al., 2020; Liu et al., 2020a) address these limitations by embedding geometric information into learnable parameters.

E Results Library

We present additional results in Figures 16 to 19. More results are available in the Supplementary Material.



Figure 16: Results Library.



Figure 17: Results Library.



Figure 18: Results Library.



Figure 19: Results Library.